Amyloid β Induces Lipid Droplet-Mediated Microglial Dysfunction in Alzheimer's Disease

Priya Prakash[1#], Palak Manchanda[1#], Evi Paouri[2], Kanchan Bisht[1], Kaushik Sharma[1], Prageeth R. Wijewardhane[1], Caitlin E. Randolph[1], Matthew G. Clark[1], Jonathan Fine[1], Elizabeth A. Thayer[1], Alexis Crockett[2], Nadia Gasmi[2], Sarah Stanko[2], Richard A. Prayson[3], Chi Zhang[1], Dimitrios Davalos[2,4*], Gaurav Chopra[1,5,6,7,8*]

[1]Department of Chemistry, Purdue University, West Lafayette, IN 47907, USA
[2]Department of Neurosciences, Lerner Research Institute, Cleveland Clinic, Cleveland, OH 44106, USA
[3]Department of Anatomic Pathology, Cleveland Clinic, Cleveland, OH 44106, USA
[4]Department of Molecular Medicine, Cleveland Clinic Lerner College of Medicine of Case, Western Reserve University, Cleveland, OH 44106, USA
[5]Purdue Institute for Integrative Neuroscience, Purdue University, West Lafayette, IN 47907, USA
[6]Purdue Institute for Drug Discovery, Purdue University, West Lafayette, IN 47907, USA
[7]Purdue Center for Cancer Research, Purdue University, West Lafayette, IN 47907, USA
[8]Purdue Institute of Inflammation, Immunology and Infectious Disease, Purdue University, West Lafayette, IN 47907, USA

[#]These authors contributed equally to this work
[*]Correspondence:
Dimitrios Davalos, Ph.D.; davalod@ccf.org
Gaurav Chopra, Ph.D.; gchopra@purdue.edu

Summary

Several microglia-expressed genes have emerged as top risk variants for Alzheimer's disease (AD). Impaired microglial phagocytosis is one of the main proposed outcomes by which these AD-risk genes may contribute to neurodegeneration, but the mechanisms translating genetic association to cellular dysfunction remain unknown. Here we show that microglia form lipid droplets (LDs) upon exposure to amyloid-beta (Aβ), and that their LD load increases with proximity to amyloid plaques in brains from human patients and the AD mouse model 5xFAD. LD formation is dependent upon age and disease progression and is more prominent in the hippocampus in mice and humans. Despite variability in LD load between microglia from male versus female animals and between cells from different brain regions, LD-laden microglia exhibited a deficit in Aβ phagocytosis. Unbiased lipidomic analysis identified a substantial decrease in free fatty acids (FFAs) and a parallel increase in triacylglycerols (TAGs) as the key metabolic transition underlying LD formation. We demonstrate that DGAT2, a key enzyme for the conversion of FFAs to TAGs, promotes microglial LD formation, is increased in microglia from 5xFAD and human AD brains, and that inhibiting DGAT2 improved microglial uptake of Aβ. These findings identify a new lipid-mediated mechanism underlying microglial dysfunction that could become a novel therapeutic target for AD.

Keywords

Microglia, lipids, lipidomics, lipid droplets, Alzheimer's disease, metabolism, neurodegeneration, phagocytosis, glia

72
73 **Introduction**
74
75 Alzheimer's disease (AD) is a progressive neurodegenerative disorder of the aging human
76 population. Accumulation of amyloid-beta (Aβ) is a defining histological hallmark of the AD
77 brain[1]. However, failures in Aβ-targeted clinical trials[2], combined with findings showing no
78 apparent correlation between cognitive decline and overall plaque load in AD patients[3], suggest
79 that additional mechanisms may be crucially involved in AD etiopathogenesis. Genome-wide
80 association studies (GWAS) identified many AD risk genes related to the immune response and
81 microglia, including the phagocytic receptors CD33 and TREM2[4,5,6,7,8]. Single-cell RNA
82 sequencing identified gene signatures characteristic of prominent protective and dysfunctional
83 microglial subpopulations in AD[9,10]. Moreover, a study that focused on human brain disease-
84 associated variants of non-coding regulatory regions in a cell-specific manner identified multiple
85 sporadic AD risk variants specifically in microglial transcriptional enhancers[11], further
86 highlighting the involvement of microglia in AD pathogenesis.
87
88 In the AD brain, reactive microglia cluster around Aβ plaques[12] and form a physical barrier
89 believed to restrict plaque propagation[13,14]. During early stages of AD, microglial reactivity is
90 considered as beneficial for Aβ clearance[15]; however, sustained inflammation likely contributes to
91 neurodegeneration[12]. Increased pro-inflammatory gene expression in response to accumulating Aβ
92 in older AD mice leads to decreased microglial Aβ clearance receptors or Aβ-degrading enzymes,
93 thereby promoting further Aβ accumulation[16]. Furthermore, the ability of microglia to remove Aβ
94 declines over time, supporting that the progression of amyloid pathology correlates with impaired
95 capacity of microglia to phagocytose Aβ[17,16].
96
97 In addition to genes and proteins, changes in microglial lipid content can also affect their state and
98 function[18,19,20,21]. Cellular lipids regulate functions like migration and phagocytosis[22], are
99 important for immune cell modulation and signaling[23], and their dysregulation has been linked to
100 neurodegenerative disorders, including AD[24]. Top AD-risk genes such as TREM2, APOE, and
101 INPP5D are directly related to lipid metabolism[25,26,27]. Although lipid droplets (LDs, first
102 described as fat particles by Alois Alzheimer[28]) were initially considered to be passive fat
103 deposits[29], they are dynamic intracellular organelles (diameter <1–100 μm) that regulate lipid
104 metabolism. LDs consist of a phospholipid monolayer containing a core of neutral lipids like
105 triacylglycerols (TAGs) and cholesteryl esters (CEs)[30]. Inflammatory triggers like
106 lipopolysaccharide (LPS)[31,19], fatty acids[32], and aging[20] can result in LD accumulation in primary
107 microglial cells and cell lines. Further, human iPSC-derived microglia were enriched in LDs in a
108 chimeric mouse model of AD[33]. However, it is not known if Aβ can directly induce LD formation
109 in microglia, and if/how changes to their lipid or metabolite composition can affect microglial
110 function in AD.
111
112 Here we show that plaque-associated microglia closely associated with Aβ plaques contained more
113 LDs and had larger cell bodies and shorter processes in both mouse and human brains, highlighting
114 a unique LD-laden microglial subtype in AD. Extensive lipidomic and metabolomic profiling in
115 microglia revealed specific types of lipids and metabolic pathways likely responsible for their LD-
116 laden phenotype in the 5xFAD mouse model, which was more pronounced in microglia from
117 females compared to males. Functionally, LD-laden microglia showed reduced phagocytosis of

3

118 Aβ compared to age-matched WT microglia. Mechanistically, we found that Aβ treatment alone
119 promotes a drastic shift in lipid content in microglia isolated from WT brains, even within only 24
120 hours of Aβ exposure. Extensive lipidomic characterization of these microglia revealed a gradual
121 increase in TAG content following Aβ treatment, which was similar to the lipid composition
122 changes we detected in microglia from 5xFAD mice. Based upon this finding, we identified
123 diacylglycerol O-acyltransferase 2 (DGAT2), a key enzyme for the conversion of FFAs to TAGs,
124 as also being the key catalyst for Aβ-induced LD formation in microglia. Importantly, DGAT2
125 protein expression was increased in both mouse and human AD brains, and inhibiting DGAT2
126 increased the phagocytosis of Aβ by 5xFAD microglia. Our study thus highlights DGAT2 as a
127 promising target for preventing or reversing phagocytic dysfunction in LD-laden microglia in the
128 AD brain.

129
130

131 **Microglia accumulate lipid droplets in an age-, sex-, and region-dependent manner in the**
132 **5xFAD model of Alzheimer's disease**

133

134 Prior literature has linked the accumulation of LDs in microglia with inflammation, aging, and
135 impaired phagocytosis, all of which are also hallmarks of AD[31,20,33]. We asked if/how exposure to
136 Aβ could induce LD formation in microglia, and/or alter their lipid or metabolite composition in a
137 way that affects their function in AD. We used a mouse model with five familial AD mutations
138 (5xFAD)[34], which progressively accumulates extensive Aβ plaques (especially in the subiculum
139 and deep cortical layers) starting around 2-3 months of age. 5xFAD mice also develop prominent
140 gliosis, inflammation, neuronal loss, behavioral impairments, and sex-distinct systemic metabolic
141 changes[35,34,36]. We isolated microglia from 5xFAD and WT mice and performed flow cytometry
142 analysis after staining for their neutral lipids (**Fig. 1a; Fig. S1a**). Although there was no difference
143 in younger mice (**Fig. 1b**), microglia from 5-7-month-old female 5xFAD mice showed
144 significantly higher LD content (1.58-fold) compared to cells from age-matched controls. Among
145 LD+ cells, almost all 5xFAD microglia had high LD content, whereas WT microglia had lower LD
146 content (**Fig. 1c**). Microglia from 5-7-month-old male 5xFAD mice also showed a significant but
147 modest increase (1.15-fold) in LDs compared to WT (**Fig. 1d**), however a higher number of LD+
148 microglia had high LD content in cells from 5xFAD compared to WT male mice (**Fig. 1e**). These
149 findings demonstrate that microglia show increased LD load, in a mouse model of AD with
150 extensive Aβ brain deposition, albeit with some age- and sex-dependent variability.

151

152 Next, we investigated if acutely-isolated microglia from 5xFAD mice showed alterations in their
153 global lipid and metabolite profiles as they experienced a drastic increase in Aβ plaque load with
154 age. We performed unbiased mass spectrometry lipidomic and metabolomic profiling using a
155 modified multiple reaction monitoring (MRM)[37] approach that allowed us to screen 1380 lipid
156 species, categorized into 10 main classes (**Fig. S1b**), and over 700 metabolites. Such broad
157 coverage and depth of profiling allowed us to explore possible differences in the lipid profiles of
158 microglia from 5-7-month-old male and female 5xFAD mice and compare them to those from age-
159 and sex-matched WT microglia in an unbiased manner (**Supplementary Tables ST1-ST2**).
160 Female 5xFAD microglia showed clearly distinct profiles, (indicated by their clear separation in
161 the principal component analysis (PCA) space, accounting for over 95% of the variation in the
162 data) (**Fig. 1f**), with 105 differentially-regulated lipids that were primarily downregulated,
163 compared to cells from WT controls (**Fig. S1c-e**).

164

165 We further evaluated triacylglycerol (TAG) profiles in female microglia and found an increase in
166 several long-chain species, including TAG(48:0), TAG(50:2), TAG(50:0), TAG(52:2),
167 TAG(52:0) in 5xFAD compared to WT cells (**Fig. 1g, Supplementary Table ST3**). In contrast,
168 the male lipidome showed less variability (poor separation in the PCA space) (**Fig. S1f**), in
169 agreement with the more limited variation in LD content in male microglia when analyzed at the
170 single-cell level (**Fig. 1d**). We also compared microglial metabolite profiles from the same tissues
171 and found them to be distinctly different (**Fig. S2a**). Metabolites like fructose 6-phosphate and
172 lactose were downregulated in 5xFAD male and female microglia compared to cells from WT
173 controls, affecting several key metabolic pathways such as the citrate TCA cycle, glutamine and
174 glutamate metabolism, arginine biosynthesis, etc. (**Fig S2b-c, Supplementary Tables ST4, ST5**).
175 These results illustrate that following prolonged Aβ exposure, microglia exhibit: i) a unique lipid
176 signature that likely facilitates the formation and accumulation of LDs within them in a sex-distinct
177 manner, and ii) dysregulation in several key metabolic pathways, that could also impact their
178 functions in the context of AD.

179

180 **Microglia have increased LD content in the hippocampus of 5xFAD mice and AD patients**

181

182 We next asked if/how the increased LD content and related metabolic changes related to brain
183 amyloid deposition, one of the prominent pathological hallmarks of 5xFAD mice and AD brains.
184 We examined the spatial distribution of LDs by performing label-free stimulated Raman scattering
185 (SRS) microscopy[38] in hippocampal brain slices of 5xFAD mice. We found a significantly higher
186 number of LDs, and a higher percentage of LD area overall, in chronic 5xFAD compared to age-
187 matched WT hippocampi (**Fig. 1h**). Interestingly, some LDs appeared in close proximity to Aβ
188 plaques in the 5xFAD tissue, as identified by their respective spectral signatures (**Fig. S3**).

189

190 To further profile the spatial distribution of LD-laden microglia relative to amyloid plaques, we
191 combined histological staining with methoxy O4 (amyloid plaques) and LipidTox (lipids) with
192 immunohistochemistry for IBA1 (microglia) in 5-7-month-old female 5xFAD brain sections. Even
193 though aged WT brains had a high number of LDs in microglia (as also previously reported[20]), and
194 in other cells (**Fig. 1i; S4a**), 5xFAD brains had significantly higher overall LD density and total
195 LD area in cortex and parts of the hippocampus (CA1 and subiculum) compared to WT (**Fig. S4b-
196 c**). The mean cell body area of LD$^+$ microglia was not significantly different than that of LD$^-$ cells
197 (**Fig. S4d**), nor was the mean cell body area of LD$^+$ microglia in 5-7-month-old female 5xFAD
198 mice compared to LD$^+$ cells in age and sex-matched WT controls (**Fig. S4e**). Similarly, the overall
199 proportion of LD$^+$ microglia was similar across cortex, CA1, and subiculum (**Fig. S4f**), but the
200 proportion of LD area within microglia was significantly increased in the subiculum of 5xFAD
201 mice (**Fig. 1j**), indicating a preferential increase in LD load within microglia in this brain region.

202

203 Since the hippocampus is significantly affected by amyloid pathology in AD patients[39], we also
204 stained postmortem human hippocampal sections from non-symptomatic (NS) and AD patients
205 for Aβ plaques, LDs, and microglia (**Fig. 1k**). After 3D reconstruction and segmentation of each
206 stained structure imaged by high-resolution confocal microscopy, we performed volumetric co-
207 localization analysis using Imaris (**Fig. S5**). We measured significantly higher (5.7-fold increase)
208 overall LD density (**Fig. 1l; Fig. S6)**, and—similar to the mouse model findings—a significantly

209 higher percentage of microglial volume occupied by LDs in the hippocampus of AD patients
210 compared to NS controls in both males and females (**Fig. 1m**).
211
212 **Chronic exposure of microglia to Aβ plaques promotes LD accumulation, alters microglial**
213 **morphology, and impairs their phagocytic ability**
214
215 We next examined the spatial relationship between plaque load and LD density and found them to
216 be positively correlated in the cortex, CA1, and subiculum (**Fig. 2a**). Interestingly, the vast
217 majority of plaque-proximal microglia were laden with LDs in all three brain regions (**Fig. 2b;**
218 **Fig. S7a**). Particularly in the subiculum, plaque-proximal microglia demonstrated an amoeboid
219 morphology, while plaque-distant cells typically had smaller cell bodies and longer processes (**Fig.**
220 **2c-d; Fig. S7b, c**). Importantly, this also translated in human microglia in the hippocampus of AD
221 patients (both male and female), where plaque-proximal microglia had a significantly higher
222 number of LDs than plaque-distant microglia, which decreased with distance from the nearest
223 plaque (**Fig. 2e, f; Fig. S7d; Supplementary Movie 1**). In addition, LD$^+$ microglia closer to
224 plaques (0-10μm) contained larger LDs, and their total LD load also decreased progressively with
225 distance from the nearest plaque (**Fig. 2g; Fig. S7e**). The methodological approach implemented
226 in Imaris to identify PLIN2$^+$IBA1$^+$ cells and their LD load as a function of distance from the nearest
227 plaque is schematically represented in **Fig S8**. Overall, these results suggest that a
228 morphologically-distinct plaque-associated microglial phenotype characterized by larger LD load
229 exists in both the human AD brain and the amyloid-rich 5xFAD animal model.
230
231 Plaque-associated microglia have been previously shown to exhibit morphological and molecular
232 differences compared to non-plaque-associated cells in AD[40,41,42]. We specifically asked if direct
233 exposure to Aβ leads to LD formation and changes to phagocytic function in microglia. Microglia
234 isolated from 5-7-month-old female 5xFAD and WT mice were acutely seeded (1 hour) and treated
235 with Aβ^{pH}—a pH-dependent fluorescent probe that emits green fluorescence in the acidic
236 lysosomes upon phagocytosis[43]; LDs were then stained with LipidTox, and all cells were analyzed
237 by flow cytometry (**Fig. 2h, Fig. S9a**). Microglia isolated from WT mice showed a significant
238 increase in LD content (4.5-fold) upon direct exposure to Aβ^{pH} (**Fig. 2i**). However, Aβ^{pH} treatment
239 did not cause a significant increase in LDs in microglia isolated from 5xFAD brains (**Fig. 2j**). This
240 could indicate that since 5xFAD mice progressively develop Aβ plaques starting at 2 months of
241 age, chronic microglial exposure to Aβ possibly alters their functional abilities and overall state
242 by the age of 5-7 months, when amyloid deposition is extensive throughout the brain.
243
244 Microglial phagocytosis of Aβ is a critical clearance mechanism, and alterations of microglial
245 phagocytic capacity have been reported in chronic inflammation and AD mouse models[15,16]. We
246 therefore investigated if the increase in microglial LDs affects their phagocytic capacity. Live
247 microglia from 5xFAD brains showed a significant (40%) reduction in Aβ^{pH} phagocytosis
248 compared to cells from WT brains (**Fig. S9b-c**). Specifically, out of all microglia, 63.55% and
249 47.92% were Aβ^{pH+} in WT and 5xFAD, respectively (**Fig. 2k**). Interestingly, LD$^+$ 5xFAD
250 microglia showed impaired phagocytosis compared to LD$^+$ WT cells (**Fig. 2l**). Surprisingly, WT
251 microglia showed an increase in LDs due to acute Aβ^{pH} but did not exhibit reduced phagocytic
252 capacity. In conclusion, these experiments demonstrate that LD-laden microglia that are
253 chronically exposed to Aβ exhibit a dysfunctional phagocytic phenotype.
254

255

Direct Aβ exposure is sufficient to significantly alter the microglial lipidome towards lipid droplet formation, independently of inflammatory factors

We were surprised to discover that in microglia from 5-7-month-old WT brains, even acute direct exposure to Aβ *ex vivo* was sufficient to induce large LD formation. Thus, we asked if direct Aβ exposure is sufficient to promote LD formation and/or regulate broad metabolic changes in microglia independently of other inflammatory factors. We isolated $CD11b^+$ primary microglia from 5-7-month-old WT mice, cultured them *in vitro* for 7-10 days and treated them with Aβ aggregates for 1, 12, and 24 hours before assaying both cellular and secretory lipids and metabolites by mass spectrometry-based MRM-profiling (**Fig. 3a**). We again screened over 1370 lipid species categorized into 10 main classes including FFAs, ceramides, and TAGs (**Supplementary Tables ST6, ST7**) as well as over 700 metabolites (**Supplementary Tables ST8, S9**). We found considerable differences in the microglial lipidome between Aβ- and vehicle-treated cells, at 1 hour and 24 hours of Aβ treatment, respectively, suggesting a distinct lipidomic transition occurring within microglia following exposure to Aβ (**Fig. 3b**).

While we observed dramatic changes in several lipid classes, FFAs were the most differentially-regulated lipid class with acute (1 hour) Aβ exposure (**Fig. 3c-d**), with very long-chain saturated FFAs, C20:0, C22:0, and C19:0 being the most upregulated lipids at this time point (**Fig. 3e; S10a**). We also used novel gas-phase ion/ion chemistry (**Supplementary Results**) to structurally validate these highly-expressed saturated FFAs and confirmed that these specific saturated FFA structures were indeed directly synthesized in microglia with acute (1 hour) Aβ exposure (**Fig. 3f, S11a-b**). Interestingly, the cells did not maintain their saturated FFA repertoire with prolonged Aβ exposure (24 hours) and transitioned to TAGs, which were the most differentially-regulated lipid class at this time point, with TAG(52:3), TAG(54:3), and TAG(52:2) being the most upregulated species (**Fig. 3c-e; S10b**). In addition, MRM-profiling confirmed the increase of specific TAGs in Aβ-treated microglia at the 24-hour time point compared to vehicle-treated microglia (**Fig. 3e, Supplementary Table ST10**). Furthermore, at 12 hours of Aβ treatment, in addition to FFAs, cholesteryl esters (CEs) were the second most differentially-regulated lipid class, with very long chain CEs 20:2, 24:1, and 16:3 being the top upregulated CEs in microglia (**Fig. S10c-e**). Neutral lipids like TAGs and CEs form the core of LDs and are involved in energy storage and fatty acid metabolism in cells. Importantly, we quantified the total amount of upregulated FFAs, CEs, and TAGs as percent change of maximum ion intensity and verified that the reduction in FFAs from 1 hour to 24 hours was followed by a concomitant increase in TAGs and CEs at 24 hours (**Fig. 3g**). This increase in core LD components suggested that the cells likely activated metabolic pathways towards LD formation. Taken together with acute treatment of Aβ *ex vivo* (**Fig. 2b**), these results suggest a direct effect of Aβ-aggregate exposure to promote LD formation in microglia. In contrast to the cellular lipidome, we did not find many lipids differentially regulated in the microglial conditioned media (secretory lipids) with Aβ treatment - none at 1 hour, five at 12 hours, and one at 24 hours, respectively (**Supplementary Table ST7**). Given that both lipids and metabolites work together to activate cellular metabolic pathways, we also evaluated changes in microglial metabolite profiles with Aβ exposure. Metabolites corresponding to alanine, aspartate, and glutamate metabolism, arginine biosynthesis, etc. were differentially regulated in microglia exposed to Aβ (**Fig. S12, Supplementary Table ST11**). The metabolome of the microglial conditioned media exhibited pronounced differences following 12 and 24 hours of Aβ exposure,

301 as seen in the PCA plots (**Fig. S13a**). Metabolites related to phenylalanine/tyrosine/tryptophan
302 biosynthesis and glycine/serine/threonine biosynthesis pathways were differentially regulated in
303 the microglial conditioned media due to Aβ (**Fig. S13b-c, Supplementary Table ST12**). Taken
304 together, the Aβ-treated cellular and secreted metabolites overlapped with metabolic pathways in
305 5xFAD compared to WT (**Fig. S2**). This suggests that Aβ plays a direct role in upregulating TAGs,
306 CEs and associated metabolites towards LD formation in AD. TAGs can be synthesized via two
307 major pathways involving the conversion of FFAs to TAGs via several intermediates: 1) the
308 glycerol phosphatase pathway or 2) the monoacylglycerol pathway (**Fig. 3h**)[44]. Since TAGs
309 constitute the major neutral lipid core of LDs and are integral to their structure and function, we
310 hypothesized that these pathways could be directly involved with the dramatic increase in TAGs
311 following Aβ exposure and likely also with LD formation in AD.
312
313 **The DGAT2 pathway is required for Aβ-induced lipid droplet formation in AD microglia,**
314 **and inhibiting it rescues microglial phagocytic impairment in AD**
315
316 The diacylglycerol O-acyltransferase (DGAT) enzymes catalyze the final rate-determining step in
317 the biosynthesis of TAGs. The DGAT2 enzyme is evolutionarily conserved across eukaryotes and
318 has the predominant and ancient function for mediating TAG synthesis from fatty acids[45]. In
319 addition, DGAT2 localizes around LDs, where it is required for LD-localized TAG
320 synthesis[46,47,48]. Thus, we investigated whether DGAT2 is involved in the formation of Aβ-induced
321 LDs in microglia (**Fig. 4a**). We immunostained 5xFAD and WT brain tissues for DGAT2, LDs,
322 Aβ plaques, and microglia. We found that LD-laden microglia surrounding the Aβ plaques
323 expressed DGAT2 in 5xFAD tissue (**Fig. 4b**). Although we found *Dgat2* mRNA to be
324 downregulated in 5xFAD microglia (**Fig. S14a**), we detected abundant DGAT2⁺ microglia in the
325 subiculum region of the 5xFAD brain (**Fig. S14b, Fig. 4c**).
326
327 Further, we used a DGAT2 inhibitor (D2i) to determine if reducing DGAT2 function affects
328 microglial LD content and Aβ-specific phagocytosis. Both WT and 5xFAD microglia showed a
329 significant decrease in LDs upon D2i treatment *in vitro* (approx. 51% and 57% decreases,
330 respectively, **Fig. 4d**). Further, there was a significant reduction in Aβ-induced LDs with D2i
331 treatment in WT microglia, thereby confirming that Aβ-induced LD formation requires the
332 DGAT2 pathway (**Fig. 4e-f, Fig. S15a**). Interestingly, we did not observe any significant
333 differences in Aβ-induced LDs with D2i treatment in 5xFAD microglia (**Fig. 4e-f, Fig. S15b**),
334 similar to our results showing that Aβ^{pH} treatment did not affect LD load in microglia isolated from
335 5xFAD brains. Together, these results suggest an underlying Aβ-induced LD saturation
336 mechanism that allows DGAT2-mediated microglial LD formation in 5xFAD brain after chronic
337 amyloid exposure *in vivo*, but prevents further LD accumulation upon additional *in vitro* Aβ
338 exposure.
339
340 Next, we examined if D2i affected microglial phagocytic capacity. LD⁺ microglia from WT brains
341 showed a slight but non-significant increase in Aβ^{pH} uptake with D2i compared to vehicle-treated
342 cells (**Fig. 4g; Fig. S15c**). In contrast, LD⁺ 5xFAD microglia showed a significant increase (1.41-
343 fold) in Aβ^{pH} uptake with D2i, which was similar to WT microglia in the presence of the inhibitor
344 (**Fig. 4h; Fig. S15f**). Furthermore, the overall phagocytic capacity of 5xFAD microglia was
345 improved with D2i treatment (**Fig. S15c**) compared to vehicle-treated cells, although again there
346 was no significant difference between WT and 5xFAD microglia in the presence of the inhibitor

8

347 (**Fig. S15d-e**). Thus, the phagocytic dysfunction of LD-laden 5xFAD microglia was attenuated in
348 the presence of D2i.
349
350 Finally, we immunostained human AD and NS hippocampal tissue for Aβ plaques, LD, DGAT2,
351 and microglia. We found that plaque-associated microglia with increased LD content exhibited
352 higher DGAT2 levels in AD brains compared to microglia from NS brains (**Fig. 4i**). In summary,
353 we have discovered a novel Aβ-mediated mechanism that promotes LD formation in microglia
354 and identified the DGAT2 pathway as a novel target for therapeutic intervention to reduce
355 phagocytic impairment of microglia and promote amyloid clearance or limit amyloid accumulation
356 in the AD brain.
357

DISCUSSION

359
360 Over the past two decades, a plethora of studies have revealed important microglial contributions
361 to practically every neurological disorder or disease, with roles ranging from protective to
362 harmful[49]. This collective body of work, together with an increasing number of microglial
363 transcriptomic profiling studies, have underscored their multidimensional nature and their
364 impressive capacity to react to any signal presented to them in an age–, sex–, disease stage–, and
365 overall context–specific manner[49]. In this study, we showed that in the context of AD pathology,
366 chronic exposure to Aβ promotes specific metabolic changes in microglia that make them
367 progressively accumulate LDs and render them incapable of contributing to Aβ clearance. LD-
368 laden microglia increase in numbers in an age- (5-7-month old), sex- (female), and brain region-
369 specific manner (subiculum) in 5xFAD mice. These microglia are closely associated with Aβ
370 plaques and have a unique morphology comprised of larger cell bodies and shorter processes in
371 both 5xFAD and human AD brains. Importantly, LD-laden microglia exhibit reduced phagocytosis
372 of Aβ, a critical functional consequence of LD accumulation. Further, by challenging primary WT
373 microglia directly with Aβ, we discovered that even acute exposure to Aβ was sufficient to shift
374 their lipidomic composition towards reduced FFA and increased TAG content – a major
375 component of LDs. We thus identified DGAT2, a key enzyme for the conversion of FFAs to TAGs,
376 as an essential mediator of LD formation in microglia, and showed its increased abundance in
377 5xFAD as well as human AD brain tissue. Crucially, pharmacological inhibition of DGAT2
378 improved Aβ phagocytosis, thus unraveling a new mechanism related to microglial dysfunction in
379 AD.
380
381 Recent studies focused on transcriptomic changes occurring in microglia at the single-cell level
382 due to Aβ. While such studies demonstrate the extent of glial heterogeneity in a specific
383 environment based upon highly-abundant and actively-transcribed genes in each subpopulation,
384 they do not fully capture the functional aspects of these cell populations, which are directly
385 determined by bioactive molecules such as proteins, lipids, and other metabolites. We performed
386 the first-ever large-scale lipidomic and metabolomic characterization of microglia with acute
387 exposure to Aβ *in vitro* and in chronic 5xFAD mice, profiling over 1300 lipid species and 700
388 metabolites. Our data, which will be made available online (http://microgliaomics-
389 chopralab.appspot.com), showed an increase in long-chain saturated FFAs (specifically C20:0,
390 C19:0, and C22:0) upon 1h Aβ exposure; however, longer treatment with Aβ (24h) resulted in an
391 abundance of long-chain TAGs. Previous studies showed that saturated FFAs are extremely
392 cytotoxic to cells[50]. One way that cells overcome FFA-induced cytotoxicity is by metabolizing

393   them into TAGs[51], which are integral components of the LD core. Microglia are thus able to
394   circumvent lipid-mediated cytotoxicity via the production and accumulation of LDs. Interestingly,
395   we recently found that reactive astrocytes secrete long-chain saturated FFAs that kill injured
396   neurons and oligodendrocytes *in vitro* and *in vivo*[37]. While injured neurons and oligodendrocytes
397   typically have a low capacity for consuming FFAs and sequestering them into LDs[52], making them
398   more vulnerable to lipid-induced cytotoxicity in chronic inflammation[53,54], our findings
399   demonstrate that microglia can metabolize these toxic molecules into TAGs. This response could
400   be one way that microglia protect themselves and neurons from the cytotoxic environment of the
401   chronically-inflamed AD brain; however, it seems to affect their own morphology and functional
402   state as well.

404   Changes in microglial morphology have been described in numerous inflammatory, degenerative,
405   and injury paradigms as indications of changes in their overall state and reactivity. In our study,
406   LD-laden microglia were closely associated with Aβ plaques and exhibited shorter processes and
407   larger cell bodies in both 5xFAD mouse and human AD brains. These unique LD-laden microglia
408   were primarily located in the hippocampal subicular regions of 5xFAD mice and in postmortem
409   human hippocampi from AD patients, which are the sites of the earliest atrophy seen during AD
410   pathogenesis[55]. In addition to the protective roles of some lipids[56], their accumulation is also linked
411   to cellular senescence[57]. For example, in an obesity mouse model, senescent glia were found to
412   accumulate LDs, which contributed to impaired neurogenesis[58]. Whether these LD-laden
413   microglia are ultimately detrimental or protective to the tissue due to their dysfunctional, hyper-
414   reactive, and/or senescent state in the context of chronic inflammation remains elusive and may
415   well depend upon the extent or nature of metabolic changes that microglia experience in the
416   context of different challenges. Overall, these observations open new avenues for exploring the
417   functional roles of plaque-associated LD-laden microglia and their involvement in AD
418   progression, as well as the functional significance of LD accumulation in microglia in other
419   neuropathologies.

421   Phagocytosis is a major innate immune mechanism contributing to Aβ clearance, and its failure
422   favors Aβ accumulation in the brain. Late-onset AD, which accounts for ~95% of AD cases, is
423   associated with impaired Aβ clearance[59]. Microglia directly engulf and degrade Aβ[60,61], but their
424   capacity for efficient phagocytosis declines with aging, chronic exposure to Aβ, and during
425   sustained inflammation in the AD brain[62,16,17]. Indeed, acute exposure of primary microglia to Aβ
426   increased their inflammatory cytokine secretion and phagocytic performance, while chronic
427   exposure reduced phagocytosis and induced immune tolerance as well as a metabolic shift from
428   oxidative phosphorylation to glycolysis[63]. Interestingly, restoration of microglial phagocytosis
429   improved cognitive function in aged mice and promoted a homeostatic microglial transcriptional
430   signature[64].

432   Plaque–associated microglia have direct access to remove aggregated amyloid through
433   phagocytosis. Prior studies have proposed that these cells are compacting amyloid plaques through
434   phagocytic receptors such as TREM2[14], (a receptor expressed on myeloid cells, for which gene
435   variants have been associated to increased AD risk)[14,8], Axl, and Mer[65]. Genetic deletion of any of
436   these receptors in mouse models of AD resulted in less compact/more diffuse plaques, and was
437   associated with increased neuritic dystrophy around Aβ deposits[14,65]. These studies suggested that
438   microglia build a neuroprotective barrier that limits plaque growth through their phagocytic

10

439   receptors, and further proposed microglia as plaque "compactors" that uptake Aβ and condense it
440   in their lysosomes to eventually re-deposit it as dense core plaques[65]. We found that plaque–
441   associated microglia progressively accumulated more LDs, and that cells with increased LD
442   content were less capable of Aβ phagocytosis. LD-laden microglia found in the aged brain also
443   demonstrated phagocytic deficits[20], but the molecular mechanisms linking the appearance of these
444   organelles with functional deficits in microglia were unclear. We discovered that Aβ alone can
445   shift the metabolic equilibrium within microglia to convert FFAs to TAGs, one of the main
446   components of LDs. To decipher if this catalytic conversion that is known to contribute to LD
447   formation[51,66] is also responsible for microglial dysfunction, we blocked DGAT2, a key enzyme
448   for this pathway. Although we found the DGAT2 mRNA significantly decreased in 5xFAD
449   microglia, the protein was abundant in plaque-associated LD-laden microglia in both mouse and
450   human AD brains, underscoring how relying solely on transcript levels might mask important
451   ongoing cellular functions. Importantly, blocking DGAT2 was sufficient to restore phagocytosis
452   in 5xFAD microglia, suggesting that phagocytic dysfunction is the consequence, rather than the
453   cause, of chronic LD accumulation and pointing towards DGAT2 as a promising target to restore
454   microglia-mediated Aβ clearance. In support of our findings, a study in macrophages showed that
455   their phagocytic function is also dependent upon the availability of FFAs that are generated upon
456   degradation of LDs, suggesting that LD accumulation somehow limits the phagocytic capacity of
457   all tissue-resident macrophages[67].
458
459   Delineating the molecular mechanisms that drive LD accumulation and their downstream impact
460   on cellular functions and overall tissue health is paramount for the design of novel therapeutic
461   strategies for AD and other neurodegenerative diseases. Here, we have identified one such
462   druggable molecule that regulates TAG formation and LD accumulation in microglia while also
463   directly impacting their function. Unlike other acyltransferases, such as GPAT and AGPAT, that
464   are upstream and involved in the glycerol phosphatase pathway, the activity of DGAT is the direct
465   rate-limiting step for the biosynthesis of TAGs[44]. Therefore, since inhibiting DGAT2 alone was
466   sufficient to improve microglial phagocytosis of Aβ, targeting DGAT2 emerges as a prime target
467   for regulating the phagocytic activity of LD-laden microglia compared to other candidate enzymes.
468   Our study thus provides proof-of-principle for pursuing DGAT2 inhibition as an ideal strategy to
469   promote the protective role of microglia in AD, possibly in other neurodegenerative diseases with
470   excessive protein aggregation and LD deposition as well.
471
472
473   **MAIN REFERENCES**
474

475   1.   Serrano-Pozo, A., Frosch, M. P., Masliah, E. & Hyman, B. T. Neuropathological
476   alterations in Alzheimer disease. *Cold Spring Harb. Perspect. Med.* **1**, (2011).
477   2.   Plascencia-Villa, G. & Perry, G. Status and future directions of clinical trials in
478   Alzheimer's disease. in *International Review of Neurobiology* vol. 154 3–50 (2020).
479   3.   Morris, G. P., Clark, I. A. & Vissel, B. Inconsistencies and Controversies Surrounding the
480   Amyloid Hypothesis of Alzheimer's Disease. *Acta Neuropathologica Communications*
481   vol. 2 1–21 (2014).
482   4.   Bertram, L. *et al.* Genome-wide Association Analysis Reveals Putative Alzheimer's
483   Disease Susceptibility Loci in Addition to APOE. *Am. J. Hum. Genet.* **83**, 623–632
484   (2008).

485   5.   Hollingworth, P. *et al.* Common variants at ABCA7, MS4A6A/MS4A4E, EPHA1, CD33
486   and CD2AP are associated with Alzheimer's disease. *Nat. Genet.* **43**, 429–436 (2011).
487   6.   Naj, A. C. *et al.* Common variants at MS4A4/MS4A6E, CD2AP, CD33 and EPHA1 are
488   associated with late-onset Alzheimer's disease. *Nat. Genet.* **43**, 436–443 (2011).
489   7.   Guerreiro, R. *et al.* TREM2 Variants in Alzheimer's Disease . *N. Engl. J. Med.* **368**, 117–
490   127 (2013).
491   8.   Jonsson, T. *et al.* Variant of TREM2 Associated with the Risk of Alzheimer's Disease .
492   *N. Engl. J. Med.* **368**, 107–116 (2013).
493   9.   Keren-Shaul, H. *et al.* A Unique Microglia Type Associated with Restricting
494   Development of Alzheimer's Disease. *Cell* **169**, 1276-1290.e17 (2017).
495   10. Krasemann, S. *et al.* The TREM2-APOE Pathway Drives the Transcriptional Phenotype
496   of Dysfunctional Microglia in Neurodegenerative Diseases. *Immunity* **47**, 566-581.e9
497   (2017).
498   11. Nott, A. *et al.* Brain cell type–specific enhancer–promoter interactome maps and disease-
499   risk association. *Science (80-.).* **366**, 1134–1139 (2019).
500   12. Wyss-Coray, T. & Rogers, J. Inflammation in Alzheimer disease-A brief review of the
501   basic science and clinical literature. *Cold Spring Harb. Perspect. Med.* **2**, a006346 (2012).
502   13. Condello, C., Yuan, P., Schain, A. & Grutzendler, J. Microglia constitute a barrier that
503   prevents neurotoxic protofibrillar Aβ42 hotspots around plaques. *Nat. Commun.* **6**, 1–14
504   (2015).
505   14. Yuan, P. *et al.* TREM2 Haplodeficiency in Mice and Humans Impairs the Microglia
506   Barrier Function Leading to Decreased Amyloid Compaction and Severe Axonal
507   Dystrophy. *Neuron* **90**, 724–739 (2016).
508   15. Heneka, M. T. *et al.* Neuroinflammation in Alzheimer's disease. *Lancet Neurol.* **14**, 388–
509   405 (2015).
510   16. Hickman, S. E., Allison, E. K. & El Khoury, J. Microglial dysfunction and defective β-
511   amyloid clearance pathways in aging alzheimer's disease mice. *J. Neurosci.* **28**, 8354–
512   8360 (2008).
513   17. Krabbe, G. *et al.* Functional Impairment of Microglia Coincides with Beta-Amyloid
514   Deposition in Mice with Alzheimer-Like Pathology. *PLoS One* **8**, (2013).
515   18. Leyrolle, Q., Layé, S. & Nadjar, A. Direct and indirect effects of lipids on microglia
516   function. *Neuroscience Letters* vol. 708 134–348 (2019).
517   19. Tremblay, M. E. *et al.* Remodeling of lipid bodies by docosahexaenoic acid in activated
518   microglial cells. *J. Neuroinflammation* **13**, 1–18 (2016).
519   20. Marschallinger, J. *et al.* Lipid-droplet-accumulating microglia represent a dysfunctional
520   and proinflammatory state in the aging brain. *Nat. Neurosci.* **23**, 194–208 (2020).
521   21. Chausse, B., Kakimoto, P. A. & Kann, O. Microglia and lipids: how metabolism controls
522   brain innate immunity. *Seminars in Cell and Developmental Biology* vol. 112 137–144
523   (2021).
524   22. Bourre, J. M. Brain lipids and ageing. in *Food for the Ageing Population: A volume in*
525   *Woodhead Publishing Series in Food Science, Technology and Nutrition* 219–251 (2008).
526   doi:10.1533/9781845695484.2.219.
527   23. Cantuti-Castelvetri, L. *et al.* Defective cholesterol clearance limits remyelination in the
528   aged central nervous system. *Science (80-.).* **359**, 684–688 (2018).
529   24. Wong, M. W. *et al.* Dysregulation of lipids in Alzheimer's disease and their role as
530   potential biomarkers. *Alzheimer's and Dementia* vol. 13 810–827 (2017).

25. Tsai, A. P. *et al.* INPP5D expression is associated with risk for Alzheimer's disease and induced by plaque-associated microglia. *Neurobiol. Dis.* **153**, 105303 (2021).

26. Wang, Y. *et al.* TREM2 lipid sensing sustains the microglial response in an Alzheimer's disease model. *Cell* **160**, 1061–1071 (2015).

27. Fitz, N. F. *et al.* Phospholipids of APOE lipoproteins activate microglia in an isoform-specific manner in preclinical models of Alzheimer's disease. *Nat. Commun.* **12**, (2021).

28. Stelzmann, R. A., Norman Schnitzlein, H. & Reed Murtagh, F. An english translation of alzheimer's 1907 paper, "über eine eigenartige erkankung der hirnrinde". *Clin. Anat.* **8**, 429–431 (1995).

29. Farese, R. V. & Walther, T. C. Lipid Droplets Finally Get a Little R-E-S-P-E-C-T. *Cell* vol. 139 855–860 (2009).

30. Fujimoto, T. & Parton, R. G. Not Just Fat: The Structure and Function of the Lipid Droplet. *Cold Spring Harb. Perspect. Biol.* **3**, 1–17 (2011).

31. Khatchadourian, A., Bourque, S. D., Richard, V. R., Titorenko, V. I. & Maysinger, D. Dynamics and regulation of lipid droplet formation in lipopolysaccharide (LPS)-stimulated microglia. *Biochim. Biophys. Acta* **1821**, 607–17 (2012).

32. Urso, C. J. & Zhou, H. Palmitic acid lipotoxicity in microglia cells is ameliorated by unsaturated fatty acids. *Int. J. Mol. Sci.* **22**, 90–93 (2021).

33. Claes, C. *et al.* Plaque-associated human microglia accumulate lipid droplets in a chimeric model of Alzheimer's disease. *Mol. Neurodegener.* **16**, 50 (2021).

34. Oakley, H. *et al.* Intraneuronal β-amyloid aggregates, neurodegeneration, and neuron loss in transgenic mice with five familial Alzheimer's disease mutations: Potential factors in amyloid plaque formation. *J. Neurosci.* **26**, 10129–10140 (2006).

35. Oblak, A. L. *et al.* Comprehensive Evaluation of the 5XFAD Mouse Model for Preclinical Testing Applications: A MODEL-AD Study. *Front. Aging Neurosci.* **13**, (2021).

36. Merlini, M. *et al.* Fibrinogen Induces Microglia-Mediated Spine Elimination and Cognitive Impairment in an Alzheimer's Disease Model. *Neuron* **101**, 1099-1108.e6 (2019).

37. Guttenplan, K. A. *et al.* Neurotoxic reactive astrocytes induce cell death via saturated lipids. *Nature* **599**, 102–107 (2021).

38. Yu, Y., Ramachandran, P. V. & Wang, M. C. Shedding new light on lipid functions with CARS and SRS microscopy. *Biochim. Biophys. Acta - Mol. Cell Biol. Lipids* **1841**, 1120–1129 (2014).

39. Deture, M. A. & Dickson, D. W. The neuropathological diagnosis of Alzheimer's disease. *Molecular Neurodegeneration* (2019) doi:10.1186/s13024-019-0333-5.

40. Itagaki, S., McGeer, P. L., Akiyama, H., Zhu, S. & Selkoe, D. Relationship of microglia and astrocytes to amyloid deposits of Alzheimer disease. *J. Neuroimmunol.* **24**, 173–182 (1989).

41. Baron, R., Babcock, A. A., Nemirovsky, A., Finsen, B. & Monsonego, A. Accelerated microglial pathology is associated with Aβ plaques in mouse models of Alzheimer's disease. *Aging Cell* **13**, 584–595 (2014).

42. Orre, M. *et al.* Isolation of glia from Alzheimer's mice reveals inflammation anddysfunction. *Neurobiol. Aging* **35**, 2746–2760 (2014).

43. Prakash, P. *et al.* Monitoring phagocytic uptake of amyloid β into glial cell lysosomes in real time. *Chem. Sci.* **12**, 10901–10918 (2021).

44. Yen, C.-L. E., Stone, S. J., Koliwad, S., Harris, C. & Farese, R. V. Thematic review

577		series: glycerolipids. DGAT enzymes and triacylglycerol biosynthesis. *J. Lipid Res.* **49**,
578		2283–301 (2008).
579	45.	Chitraju, C., Walther, T. C. & Farese, R. V. The triglyceride synthesis enzymes DGAT1
580		and DGAT2 have distinct and overlapping functions in adipocytes. *J. Lipid Res.* **60**, 1112–
581		1120 (2019).
582	46.	Wilfling, F. *et al.* Triacylglycerol synthesis enzymes mediate lipid droplet growth by
583		relocalizing from the ER to lipid droplets. *Dev. Cell* **24**, 384–399 (2013).
584	47.	Kuerschner, L., Moessinger, C. & Thiele, C. Imaging of lipid biosynthesis: How a neutral
585		lipid enters lipid droplets. *Traffic* **9**, 338–352 (2008).
586	48.	Stone, S. J. *et al.* The endoplasmic reticulum enzyme DGAT2 is found in mitochondria-
587		associated membranes and has a mitochondrial targeting signal that promotes its
588		association with mitochondria. *J. Biol. Chem.* **284**, 5352–5361 (2009).
589	49.	Uriarte Huarte, O., Richart, L., Mittelbronn, M. & Michelucci, A. Microglia in Health and
590		Disease: The Strength to Be Diverse and Reactive. *Frontiers in Cellular Neuroscience*
591		vol. 15 (2021).
592	50.	Gordon, G. B. Saturated free fatty acid toxicity. II. Lipid accumulation, ultrastructural
593		alterations, and toxicity in mammalian cells in culture. *Exp. Mol. Pathol.* **27**, 262–276
594		(1977).
595	51.	Listenberger, L. L. *et al.* Triglyceride accumulation protects against fatty acid-induced
596		lipotoxicity. *Proc. Natl. Acad. Sci.* **100**, 3077–3082 (2003).
597	52.	Schönfeld, P. & Reiser, G. Why does brain metabolism not favor burning of fatty acids to
598		provide energy-Reflections on disadvantages of the use of free fatty acids as fuel for brain.
599		*Journal of Cerebral Blood Flow and Metabolism* vol. 33 1493–1499 (2013).
600	53.	Sultana, R., Perluigi, M. & Butterfield, D. A. Lipid peroxidation triggers
601		neurodegeneration: A redox proteomics view into the Alzheimer disease brain. *Free*
602		*Radical Biology and Medicine* vol. 62 157–169 (2013).
603	54.	Reynolds, I. J. & Hastings, T. G. Glutamate induces the production of reactive oxygen
604		species in cultured forebrain neurons following NMDA receptor activation. *J. Neurosci.*
605		**15**, 3318–3327 (1995).
606	55.	Carlesimo, G. A. *et al.* Atrophy of presubiculum and subiculum is the earliest
607		hippocampal anatomical marker of Alzheimer's disease. *Alzheimer's Dement.*
608		*(Amsterdam, Netherlands)* **1**, 24–32 (2015).
609	56.	Li, N., Lizardo, D. Y. & Atilla-Gokcumen, G. E. Specific Triacylglycerols Accumulate
610		via Increased Lipogenesis during 5-FU-Induced Apoptosis. *ACS Chem. Biol.* **11**, 2583–
611		2587 (2016).
612	57.	Lizardo, D. Y., Lin, Y. L., Gokcumen, O. & Atilla-Gokcumen, G. E. Regulation of lipids
613		is central to replicative senescence. *Mol. Biosyst.* **13**, 498–509 (2017).
614	58.	Ogrodnik, M. *et al.* Obesity-Induced Cellular Senescence Drives Anxiety and Impairs
615		Neurogenesis. *Cell Metab.* **29**, 1061-1077.e8 (2019).
616	59.	Mawuenyega, K. G. *et al.* Decreased clearance of CNS β-amyloid in Alzheimer's disease.
617		*Science (80-.).* **330**, 1774 (2010).
618	60.	Liu, Z., Condello, C., Schain, A., Harb, R. & Grutzendler, J. CX3CR1 in microglia
619		regulates brain amyloid deposition through selective protofibrillar amyloid-β
620		phagocytosis. *J. Neurosci.* **30**, 17091–17101 (2010).
621	61.	Mandrekar, S. *et al.* Microglia mediate the clearance of soluble aβ through fluid phase
622		macropinocytosis. *J. Neurosci.* **29**, 4252–4262 (2009).

623 62. Njie, e. M. G. *et al.* Ex vivo cultures of microglia from young and aged rodent brain
624   reveal age-related changes in microglial function. *Neurobiol. Aging* **33**, 195.e1-195.e12
625   (2012).
626 63. Baik, S. H. *et al.* A Breakdown in Metabolic Reprogramming Causes Microglia
627   Dysfunction in Alzheimer's Disease. *Cell Metab.* **30**, 493-507.e6 (2019).
628 64. Pluvinage, J. V. *et al.* CD22 blockade restores homeostatic microglial phagocytosis in
629   ageing brains. *Nature* **568**, 187–192 (2019).
630 65. Huang, Y. *et al.* Microglia use TAM receptors to detect and engulf amyloid β plaques.
631   *Nat. Immunol.* **22**, 586–594 (2021).
632 66. Castoldi, A. *et al.* Triacylglycerol synthesis enhances macrophage inflammatory function.
633   *Nat. Commun.* **11**, (2020).
634 67. Chandak, P. G. *et al.* Efficient phagocytosis requires triacylglycerol hydrolysis by adipose
635   triglyceride lipase. *J. Biol. Chem.* **285**, 20192–20201 (2010).
636 68. Bohlen, C. J., Bennett, F. C. & Bennett, M. L. Isolation and Culture of Microglia. *Curr.*
637   *Protoc. Immunol.* **125**, e70 (2019).
638 69. Prakash, P., Lantz, T. C., Jethava, K. P. & Chopra, G. Rapid, Refined, and Robust Method
639   for Expression, Purification, and Characterization of Recombinant Human Amyloid beta
640   1-42. *Methods Protoc.* **2**, 48 (2019).
641 70. Bligh E. G. and Dyer W. J. A Rapid Method Of Total Lipid Extraction and Purification.
642   *Can. J. Biochem. Physiol.* **37**, 911–917 (1959).
643 71. Xie, Z., Ferreira, C. R., Virequ, A. A. & Cooks, R. G. Multiple reaction monitoring
644   profiling (MRM profiling): Small molecule exploratory analysis guided by chemical
645   functionality. *Chem. Phys. Lipids* **235**, 105048 (2021).
646 72. Cordeiro, F. B. *et al.* Multiple reaction monitoring (MRM)-profiling for biomarker
647   discovery applied to human polycystic ovarian syndrome. *Rapid Commun. Mass*
648   *Spectrom.* **31**, 1462–1470 (2017).
649 73. de Lima, C. B. *et al.* Comprehensive lipid profiling of early stage oocytes and embryos by
650   MRM profiling. *J. Mass Spectrom.* **53**, 1247–1252 (2018).
651 74. Fahy, E. *et al.* Update of the LIPID MAPS comprehensive classification system for lipids.
652   *J. Lipid Res.* **50**, S9–S14 (2009).
653 75. Guttenplan, K. A. *et al.* Neurotoxic reactive astrocytes induce cell death via saturated
654   lipids. *Nature* 1–6 (2021).
655 76. Robinson, M. D., McCarthy, D. J. & Smyth, G. K. edgeR: A Bioconductor package for
656   differential expression analysis of digital gene expression data. *Bioinformatics* **26**, 139–
657   140 (2009).
658 77. McCarthy, D. J., Chen, Y. & Smyth, G. K. Differential expression analysis of multifactor
659   RNA-Seq experiments with respect to biological variation. *Nucleic Acids Res.* **40**, 4288–
660   4297 (2012).
661 78. Benjamini, Y. & Hochberg, Y. Controlling the False Discovery Rate: A Practical and
662   Powerful Approach to Multiple Testing. *J. R. Stat. Soc. Ser. B* **57**, 289–300 (1995).
663 79. Randolph, C. E., Foreman, D. J., Blanksby, S. J. & McLuckey, S. A. Generating Fatty
664   Acid Profiles in the Gas Phase: Fatty Acid Identification and Relative Quantitation Using
665   Ion/Ion Charge Inversion Chemistry. *Anal. Chem.* **91**, 9032–9040 (2019).
666 80. Randolph, C. E., Marshall, D. L., Blanksby, S. J. & McLuckey, S. A. Charge-switch
667   derivatization of fatty acid esters of hydroxy fatty acids via gas-phase ion/ion reactions.
668   *Anal. Chim. Acta* **1129**, 31–39 (2020).

669   81.   Xia, Y., Wu, J., McLuckey, S. A., Londry, F. A. & Hager, J. W. Mutual storage mode
670   ion/ion reactions in a hybrid linear ion trap. *J. Am. Soc. Mass Spectrom.* **16**, 71–81 (2005).
671   82.   Xia, Y., Liang, X. & McLuckey, S. A. Pulsed dual electrospray ionization for ion/ion
672   reactions. *J. Am. Soc. Mass Spectrom.* **16**, 1750–1756 (2005).
673   83.   Londry, F. A. & Hager, J. W. Mass selective axial ion ejection from a linear quadrupole
674   ion trap. *J. Am. Soc. Mass Spectrom. 2003 1410* **14**, 1130–1147 (2003).
675   84.   Xia, J., Wishart, D. S. & Valencia, A. MetPA: a web-based metabolomics tool for
676   pathway analysis and visualization. *Bioinformatics* **26**, 2342–2344 (2010).
677   85.   Randolph, C. E., Foreman, D. J., Betancourt, S. K., Blanksby, S. J. & McLuckey, S. A.
678   Gas-Phase Ion/Ion Reactions Involving Tris-Phenanthroline Alkaline Earth Metal
679   Complexes as Charge Inversion Reagents for the Identification of Fatty Acids. *Anal.*
680   *Chem.* (2018) doi:10.1021/acs.analchem.8b03441.
681   86.   Randolph, C. E., Shenault, D. M., Blanksby, S. J. & Mcluckey, S. A. Localization of
682   Carbon-Carbon Double Bond and Cyclopropane Sites in Cardiolipins via Gas-Phase
683   Charge Inversion Reactions. *J. Am. Soc. Mass Spectrom.* (2021)
684   doi:10.1021/jasms.0c00348.

685
686
DATA AVAILABILITY
688   Supplemental tables, figures, and associated content is available with the manuscript. All data
689   analysis is available on GitHub (https://github.com/chopralab/microglia_omics). A web
690   application has been developed for exploring lipid and metabolite mass spectrometry data that will
691   be publicly available at http://microgliaomics-chopralab.appspot.com (for review, username:
692   admin, password: Review). The accession information for raw lipid and metabolite mass
693   spectrometry data is MassIVE MSV000089458:
694   https://massive.ucsd.edu/ProteoSAFe/dataset.jsp?task=0f7bd7cfaf504869bfac786e4184105e.

695
CODE AVAILIBILITY
697   All of the analysis codes for the lipidomics and metabolomics experiments are available on Github
698   at https://github.com/chopralab/microglia_omics.

699
ACKNOWLEDGEMENTS

726
727

728 **DECLARATION OF INTERESTS**
729 G.C. is the Director of the Merck-Purdue Center for Measurement Science funded by Merck Sharp
730 & Dohme, a subsidiary of Merck and a co-founder of Meditati Inc., a startup developing smart
731 drugs for mental health indications. The remaining authors declare no competing interests.
732

FIGURES
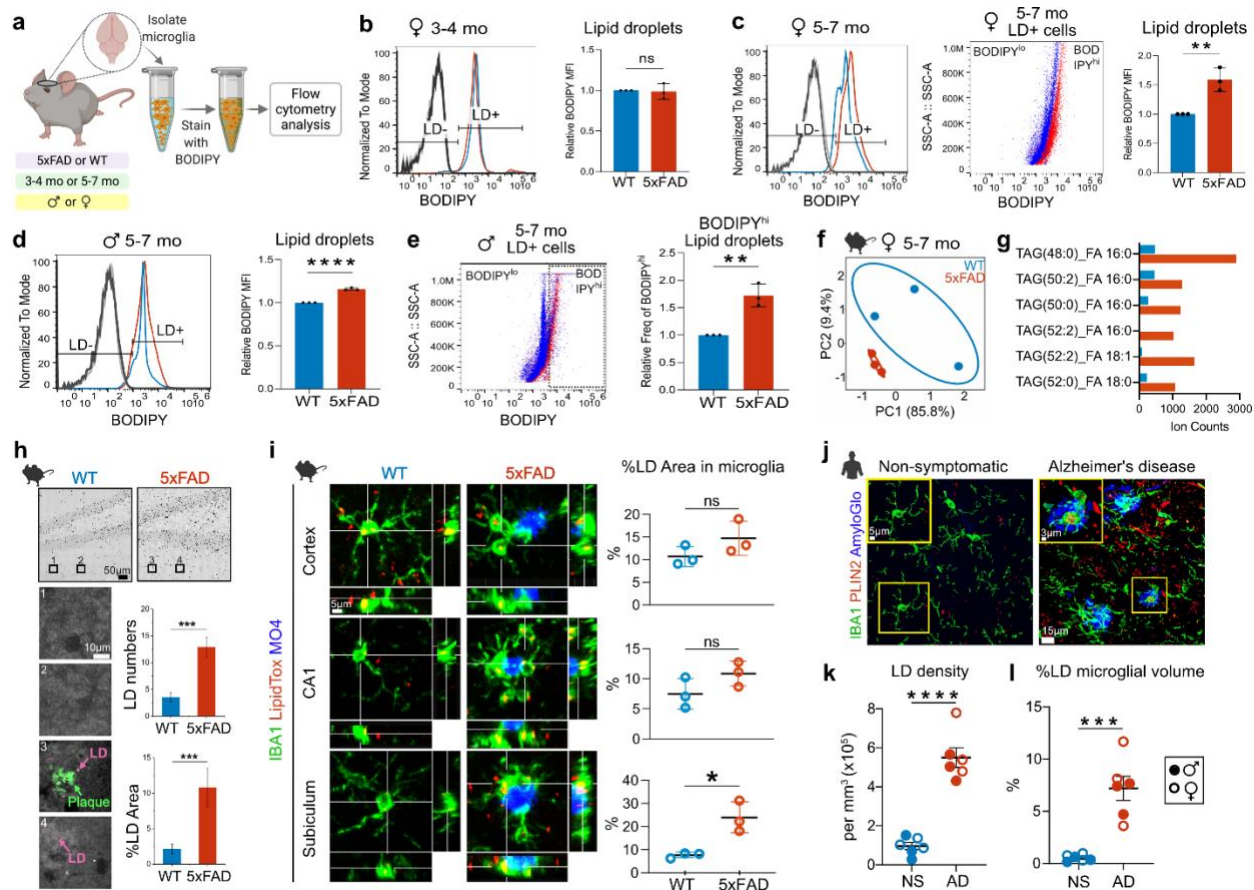
Fig. 1: LD abundance in microglia is age-, sex-, and region-dependent in the AD brain

a. Experimental design for labeling and quantifying LDs in acutely-isolated microglia from 5xFAD and WT male and female mice at 3-4 or 5-7 months old. LDs were labeled with BODIPY dye and quantified using flow cytometry. **b.** Representative graph (left) and quantification (right) of median fluorescence intensity (MFI) of LDs in live microglia (CD11b$^+$DAPI$^-$) from 3-4-month-old female mice show no increase in LD content in cells from 5xFAD (red line and bar) compared to WT animals (blue line and bar). Data represent mean ± SD. Unpaired t-test, N=3 separate experiments, each including one WT and one 5xFAD mouse. **c.** Quantification of LDs in microglia from 5-7-month-old female mice shows an increase (shift towards higher BODIPY fluorescence intensity) in LDs from 5xFAD (red) compared to WT (blue) microglia. Dot plot shows a homogeneous population of BODIPY^{hi} microglia within the LD$^+$ cell subset from 5xFAD mice (red dots) compared to microglia from WT mice (blue dots); **P= 0.0068. **d.** Quantification of LDs in microglia from 5-7-month-old male mice shows an increase in LD content in 5xFAD microglia compared to WT; ****P= 0.00003. **e.** Comparison between BODIPY^{hi} and BODIPY^{lo} cell populations within LD$^+$ microglia from 5-7-month-old male mice shows more BODIPY^{hi} microglial cells in 5xFAD mice (red dots) compared to microglia from WT mice (blue dots). Quantification shows the relative frequency of microglia containing LDs in the BODIPY^{hi} gate in 5xFAD and WT microglia; **P= 0.0039. For **c-e**: Data represent mean ± SD. Unpaired t-test, N=3

18

756 separate experiments, each including two WT and two 5xFAD mice. **f.** Principal component
757 analysis (PCA) plot depicts a clear separation based upon variation in microglial lipidomes from
758 5-7-month-old WT and 5xFAD female mice. **g.** Graph shows the identification and relative
759 amounts of specific TAG lipid species that were increased in microglia from 5-7-month-old female
760 5xFAD mice compared to cells from WT controls. For **f-g:** N=3 separate experiments, each from
761 one WT and one 5xFAD mouse. **h.** Label-free SRS imaging of LDs and Aβ plaques in 5xFAD and
762 WT brain hippocampal slices. Increased LDs were observed and quantified in 5xFAD brain
763 sections, often associated with Aβ plaques (3, 4), compared to WT tissues (1, 2). Twelve areas
764 were quantified for each group (WT and 5xFAD), from the same brain section. Unpaired t-test,
765 N=2 separate experiments, each including one WT and one 5xFAD mouse. **i.** Immunofluorescence
766 of IBA1, and counter-staining for LDs (LipidTox), and Aβ plaques (Methoxy XO4; MO4) in the
767 cortex, CA1, and subiculum regions from 5xFAD and WT mice. Quantification showed a trend
768 towards increased % LD area within microglia in the cortex and CA1 regions, which was
769 statistically significant in the subiculum (*P= 0.0147) from 5xFAD compared to WT mice. Data
770 represent mean ± SD. Unpaired t-test, N=3 separate experiments, each including one WT and one
771 5xFAD mouse. **j.** Detection of lipid droplets in human hippocampal formalin-fixed paraffin-
772 embedded (FFPE) tissue from AD and non-symptomatic (NS) cases. Immunofluorescence was
773 performed on 15µm sections for the detection of lipid droplets (PLIN2), Aβ plaques (AmyloGlo),
774 and microglia (IBA1). Representative images show an increase in the density of PLIN2$^+$ LDs in
775 AD compared to non-symptomatic cases. Higher magnification inserts show an increase of LDs
776 in microglia from AD patients compared to NS individuals. **k.** Quantification of the number of
777 PLIN2$^+$ LDs per mm^3 of imaged volume (LD density) shows a significant increase in AD
778 compared to NS cases; ****P= 0.000007. **l.** Quantification of percentage of microglial volume
779 occupied by LDs over the total microglial volume per imaged volume of hippocampal tissue shows
780 an increase in AD compared to NS cases; ***P= 0.0002. For **k**, **l**: quantification was performed in
781 3D reconstructed confocal z-stacks using Imaris; Data represent mean ± SEM. Unpaired t-test,
782 N=6 (3 males and 3 females) per group.
783
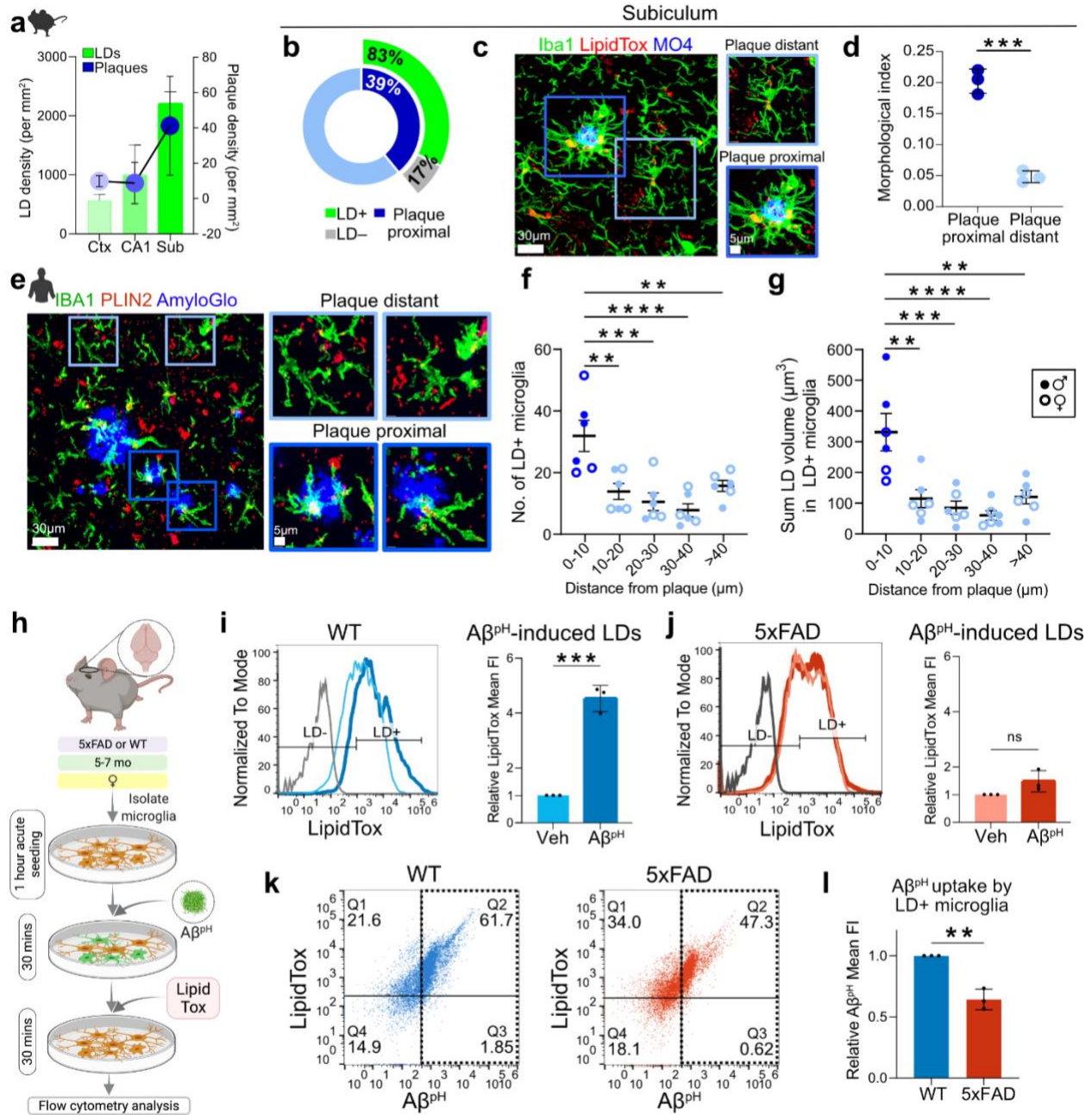
Fig. 2: LD-laden microglia exhibit phagocytosis deficits and are in close proximity to amyloid plaques in mice and humans.

a. Parallel quantification in three different 5xFAD brain regions, shows that LD density seems to correlate with plaque density, with the subiculum area of the hippocampus (Sub) where plaque density is highest also demonstrating the highest LD density compared to CA1 or cortex (Ctx). Data represent mean ± SD. N=3 5xFAD mice. **b.** Quantification of % LD^+ microglia that are plaque-proximal or -distant in the subiculum of 5xFAD mice. Out of all microglia, 39% were in contact with plaques, while 61% were away from plaques. Out of plaque-proximal microglia, 83% were LD^+, whereas only 17% were LD^-. N=3 5xFAD mice. **c.** In the subiculum of 5xFAD mice,

20

microglia (IBA1, green) exhibited larger cell bodies, shorter processes, and higher LD content (LipidTox, red) when in close proximity to Aβ plaques (MO4, blue), compared to plaque-distant microglia. **d.** Quantification showed a significantly higher morphological index in plaque-proximal compared to plaque-distant microglia in the 5xFAD subiculum; ***$P= 0.0003$. Data represent mean ± SD. Unpaired t-test, N=3 5xFAD mice. **e.** Immunofluorescence for lipid droplets (PLIN2), amyloid plaques (AmyloGlo), and microglia (IBA1) revealed larger LD volume in plaque-proximal microglia in the hippocampus of AD patients compared to plaque-distant microglia. **f.** The average number of IBA1$^+$ microglial fragments containing LDs per AD patient, was significantly increased within 10μm from the closest amyloid plaque compared to LD$^+$ microglial fragments detected 10-20μm (**$P= 0.003095$), 20-30μm (***$P= 0.000455$), 30-40μm ($P= 0.000095$) or >40μm (**$P= 0.008647$) from the closest amyloid plaque. **g.** The sum volume of all LDs within LD$^+$ microglial fragments was larger in cells located within 10μm from the closest amyloid plaque compared to LD$^+$ microglial fragments detected 10-20μm (**$P= 0.001158$), 20-30μm (***$P= 0.000241$), 30-40μm (****$P= 0.000065$) or >40μm (**$P= 0.001545$) from the closest amyloid plaque. For **f-g**: Data represent mean ± SEM. One-way ANOVA with Tukey's multiple comparison tests, N=6 AD cases (3 males and 3 females). Individual values shown were averaged from 4 z-stacks imaged per patient. **h.** Experimental design for determining the phagocytic capacity and LD load of microglia from 5xFAD and WT female mice (5-7 months old). Microglia were isolated from mouse brains, acutely seeded onto the culture plates for 1 hour, treated with the Aβ^{pH} probe for 30 mins, and with the LipidTox dye for another 30 mins before flow cytometry analysis. **i.** Quantification of LDs in Aβ^{pH}- (blue) or vehicle-treated (cyan) microglia from WT mice with fluorescence minus one (FMO) Aβ^{pH} only control (grey). Aβ^{pH} treatment induced an increase in LDs in WT microglia; ***$P= 0.0002$. **j.** Quantification of LDs in Aβ^{pH}- (red) or vehicle-treated (pink) microglia from 5xFAD mice with FMO Aβ^{pH} only control (charcoal). Aβ^{pH} treatment did not induce an increase in LDs in 5xFAD microglia. **k.** Representative dot plots showing LD and Aβ^{pH} uptake by microglia from WT and 5xFAD mice. Microglia from 5xFAD mice showed reduced Aβ^{pH} uptake compared to microglia from WT mice. **l.** Quantification of Aβ^{pH} uptake showed a phagocytic deficit in LD$^+$ microglia from 5xFAD compared to LD$^+$ microglia from WT mice; **$P= 0.0019$. For **i, j** and **l**: Data represent mean ± SD. Unpaired t-tests, cells were pooled from 3 mice per group (3 WT and 3 5xFAD mice) for each of the N=3 experiments.
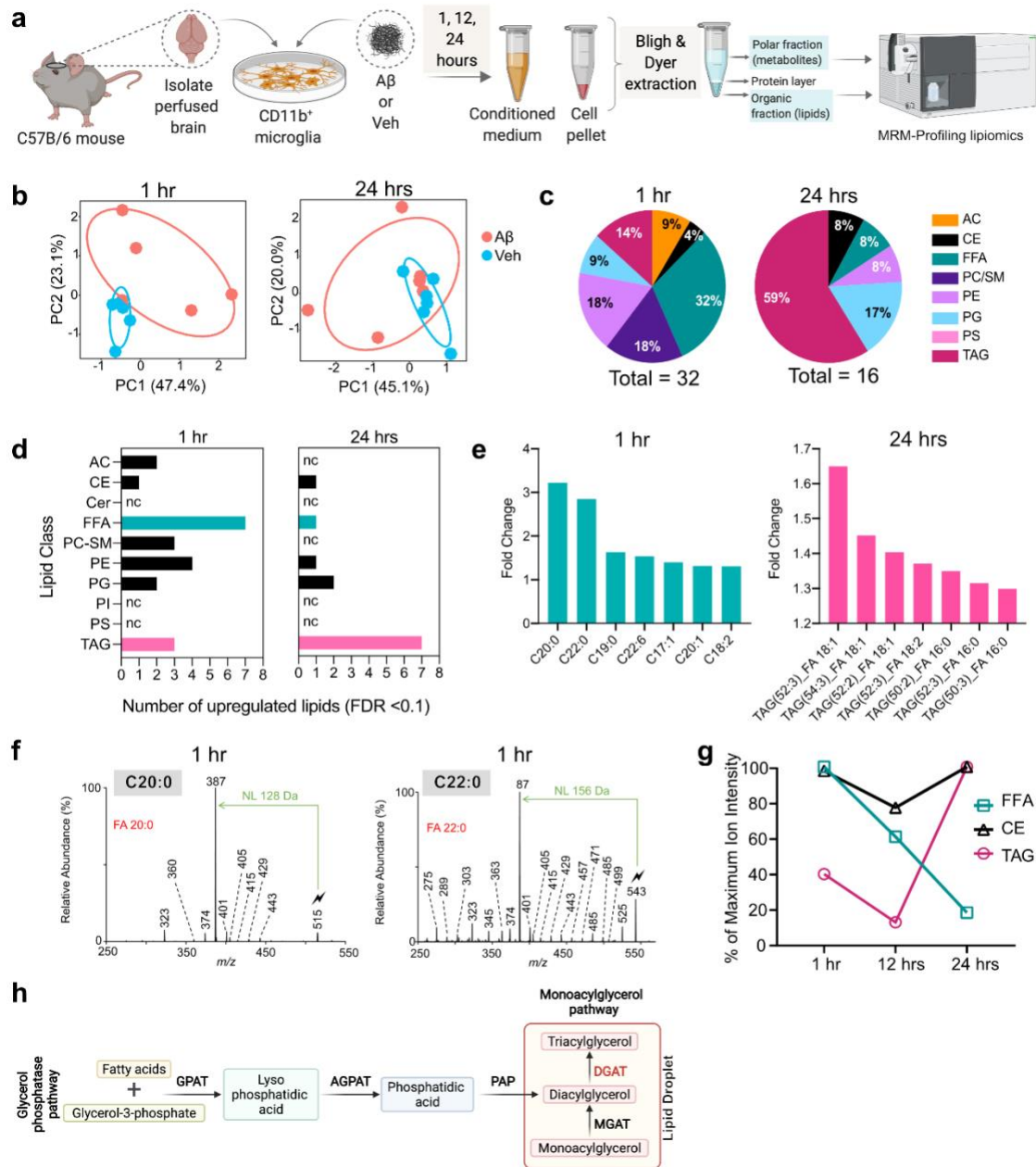
**Fig. 3: Aβ induces profound changes to the microglial lipidome and metabolome *in vitro*, resulting in LD formation.**

a. Experimental design for the global lipidomic profiling experiment performed on Aβ- and vehicle-treated primary mouse microglia. Cells were isolated from ~7-month-old C56BL/6J perfused mouse brains and cultured in growth medium containing TGF-β, IL-34, and cholesterol. Cells isolated from each brain were split and treated with 500 nM Aβ or vehicle for 1, 12, and 24 hours, followed by lipid and metabolite extraction from conditioned media and cell pellets, which were run on the Agilent triple quadrupole mass spectrometer. Lipids and metabolites were identified in the samples using MRM-profiling. Each experiment was repeated 5 or 6 times

22

837   resulting in: N=5 mice were used for 1-hour treatments, N=6 mice for 12 hours, and N=6 mice
838   for 24 hours treatments. **b.** PCA demonstrating the variation in microglial lipidomes both within
839   and between groups (Aβ or vehicle treated microglia) at 1 and 24 hours of treatment. **c.** The
840   distribution of significantly different lipid classes identified in microglia at 1 and 24 hours of Aβ
841   treatment, compared to vehicle treated cells. 32% of the differentially regulated lipids at 1 hour
842   were FFA, whereas 59% of the differentially regulated lipids at 24 hours were TAGs. **d.**
843   Upregulated lipid classes at 1 and 24 hours of Aβ treatment compared to vehicle, showed FFAs
844   and TAGs were the most abundant lipids, respectively. **e.** Individual lipid species belonging to
845   FFAs and TAGs that were upregulated at 1 and 24 hours of Aβ treatment, compared to vehicle.
846   Long-chain saturated FFAs C20:0, C22:0, and C19:0 were the top 3 upregulated FFAs within the
847   first 1-hour of Aβ treatment, while neutral lipids TAG(52:3)_FA 18:1, TAG(54:3)_FA 18:1, and
848   TAG(52:2)_FA 18:1 were the top three upregulated TAGs with prolonged 24-hour Aβ treatment,
849   both compared to vehicle. **f.** Structural identification and confirmation of the C20:0 and C22:0
850   lipids in the 1-hour Aβ-treated microglial samples, using the gas-phase ion/ion chemistry (see
851   **Supplementary Results**). **g.** Percentage changes of maximum ion intensities as a quantitative
852   measure of changes in the respective amounts of FFAs (green), TAGs (magenta), and CEs (black)
853   in microglial cells at 1, 12, and 24 hours of Aβ treatment. The reduction in FFAs was followed by
854   an increase in TAGs and CEs – major components of LDs – suggesting a gradual conversion of
855   FFAs to TAGs towards LD formation. **h.** Convergent pathways for TAG biosynthesis. Glycerol-
856   3-phosphate acyltransferase (GPAT); acylglycerol-3-phosphate acyltransferase (AGPAT);
857   phosphatidic acid phosphatase (PAP); monoacylglycerol acyltransferase (MGAT); and the final
858   rate-limiting enzyme diacylglycerol acyltransferase (DGAT) that is needed for TAGs production
859   and is involved in LD formation.
860
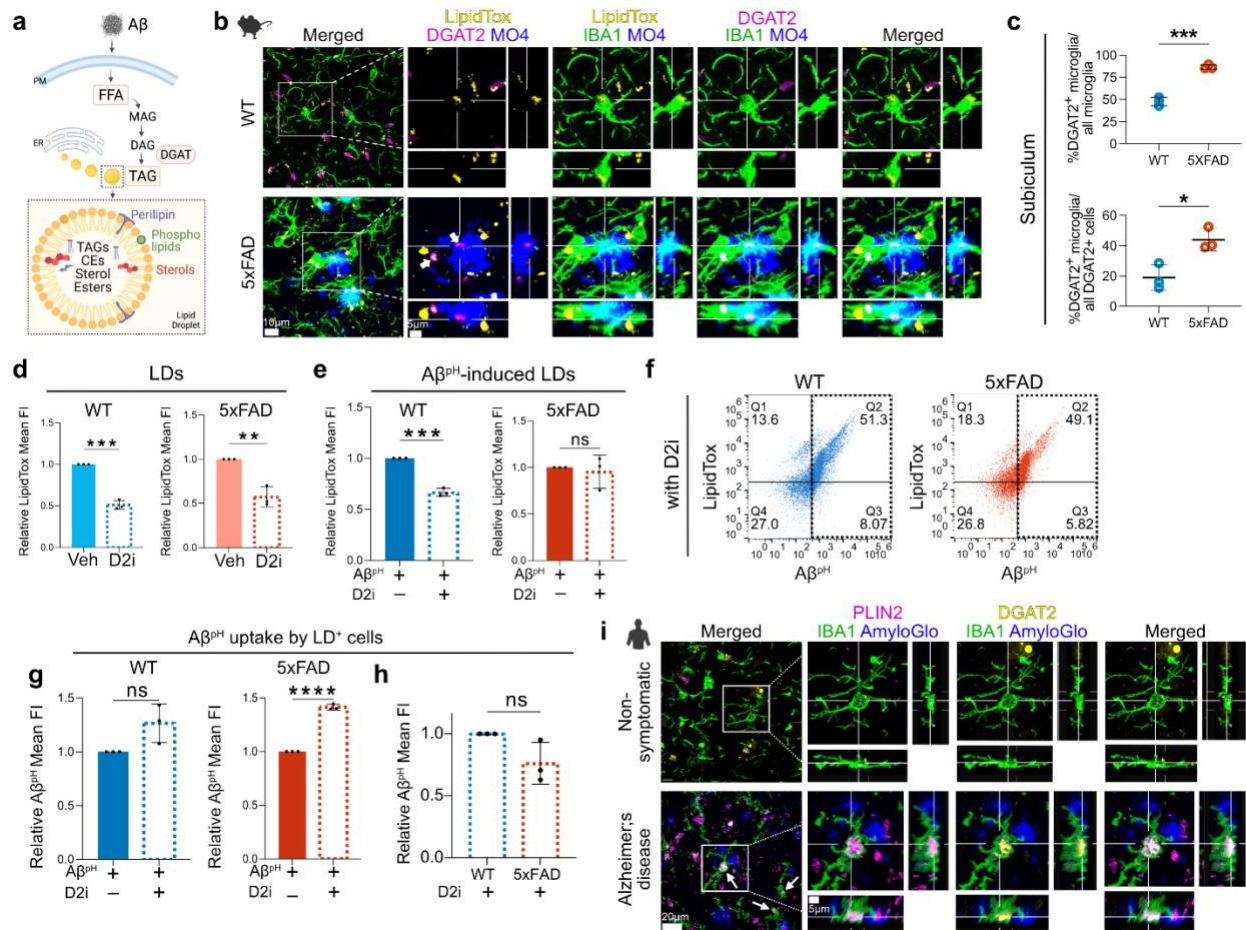
Fig. 4: The DGAT2 enzyme is required for Aβ-induced LD formation, and inhibiting it restores Aβ phagocytosis in microglia.

a. Proposed mechanism for Aβ-induced LD formation in microglia. Microglial exposure to Aβ induces an upregulation of FFAs that are converted to TAGs within LDs via the DGAT2 pathway. **b.** Immunofluorescence staining of microglia (IBA1), LDs (LipidTox), DGAT2, and Aβ plaques (MO4) in the hippocampal subicular region of 5xFAD and WT mouse brains. Increased DGAT2 is shown in microglia associated with amyloid plaques. **c.** Quantification showing a significant increase in % of DGAT2$^+$ microglia out of all microglia and out of all DGAT2$^+$ cells in the mouse subiculum in the 5xFAD tissue vs. WT; *$P= 0.0181$, ***$P= 0.0002$. Data represent mean ± SD. Unpaired t-test, N=3 mice per group. **d.** DGAT2 inhibitor (D2i) treatment reduced LDs in cultured microglia from WT and 5xFAD brains; ***$P= 0.0001$, **$P= 0.0029$. **e.** Quantification showed that D2i treatment reduced LD formation upon Aβ exposure in microglia from WT mice but not in cells from 5xFAD mice; ***$P= 0.0001$. **f.** Representative dot plots showing LD and Aβ^{pH} uptake by microglia treated with D2i from WT and 5xFAD mice. **g.** LD$^+$ microglia from WT mice showed a slight but non-significant increase in Aβ^{pH} uptake with D2i, while LD+ microglia from 5xFAD mice showed a significant increase in Aβ^{pH} uptake with D2i; ****$P= 0.000014$. **h.** Direct comparison of the effect of D2i treatment on Aβ^{pH} uptake by LD$^+$ microglia from WT and 5xFAD showed that inhibiting DGAT2 restored the phagocytic performance of 5xFAD microglia, making it comparable to that of WT cells. For **d, e, g** and **h**: Data represent mean ± SD. Unpaired t-tests,

24

882   cells were pooled from 3 mice per group (3 WT and 3 5xFAD mice) for each of the N=3
883   experiments. **i.** DGAT2 expression in LD$^+$ microglia in close proximity to amyloid plaques in
884   hippocampal FFPE tissue from human AD and NS cases (N=4 per group). Immunofluorescence
885   was performed on 15µm-thick human hippocampal sections for the detection of DGAT2, lipid
886   droplets (PLIN2), amyloid plaques (AmyloGlo) and microglia (IBA1). Increased DGAT2 signal
887   (yellow) was detected in plaque-proximal LD$^+$ microglia in AD cases (arrows), compared to NS
888   controls. Cross-sections of the selected microglial cells in the white boxes demonstrate
889   representative example of increased DGAT2 signal in close proximity to a large PLIN2-labeled
890   LD inside a plaque-proximal microglial cell in AD, and of a cell from a non-symptomatic case.
891
892

SUPPLEMENTARY TABLE LEGENDS

Supplementary Table ST1: Analyzed lipidomics data of 5xFAD vs. WT microglia, including female and male samples. Tables show the differential lipid profiles in 5xFAD vs. WT microglia samples, organized by most to least differentially-expressed lipids. Samples N1, N2, N3 belong to female mice and samples N4, N5 belong to male mice. P and FDR values are also provided and lipids with FDR<0.1 were considered to be significant.

Supplementary Table ST2: Analyzed lipidomics data of 5xFAD vs. WT microglia, female only. Table shows the differential lipid in 5xFAD vs. WT female microglia samples, organized by most to least differentially-expressed lipids. P and FDR values are also provided and lipids with FDR<0.1 were considered to be significant.

Supplementary Table ST3: Raw MRM lipidomics data of 5xFAD vs. WT microglia. Table lists the MRM transitions screened for TAGs and the respective ion intensity values, organized by MRM transition.

Supplementary Table ST4: Analyzed metabolomics data for 5xFAD vs. WT microglia (male and female). Tables show the differential metabolites in 5xFAD vs. WT microglia, organized by most to least differentially-expressed metabolites. P and FDR values are also provided and metabolites with FDR<0.1 were considered to be significant.

Supplementary Table ST5: Pathway analysis for 5xFAD vs. WT microglial metabolites. A list of all pathways matched to the differentially-expressed metabolites (FDR<0.1) is provided in the table. The pathways with P<0.05 were considered to be significant and are highlighted in the scatter plots in the supplementary figures.

Supplementary Table ST6: Analyzed lipidomics data for Aβ- vs. vehicle-treated primary microglial cells at 1, 12, and 24 hours. Tables show the differential lipid profiles in Aβ- vs. vehicle-treated cells at the three different time points, organized by most to least differentially-expressed lipids. P and FDR values are also provided and lipids with FDR<0.1 were considered to be significant.

Supplementary Table ST7: Analyzed lipidomics data of Aβ- vs. vehicle-treated primary microglial cell conditioned media at 1, 12, and 24 hours. Tables show the differential lipid profiles in Aβ- vs. vehicle-treated conditioned media samples at the three different time points, organized by most to least differentially-expressed lipids. P and FDR values are also provided and lipids with FDR<0.1 were considered to be significant.

Supplementary Table ST8: Analyzed metabolomics data of Aβ- vs. vehicle-treated primary microglial cells at 1, 12, and 24 hours. Tables show the differential metabolites in Aβ- vs. vehicle-treated cells at the three different time points, organized by most to least differentially-expressed metabolites. P and FDR values are also provided and metabolites with FDR<0.1 were considered to be significant.

Supplementary Table ST9: Analyzed metabolomics data of Aβ- vs. vehicle-treated primary microglial cell conditioned media at 1, 12, and 24 hours. Tables show the differential metabolites in Aβ- vs. vehicle-treated conditioned media samples at the three different time points, organized by most to least differentially-expressed metabolites. P and FDR values are also provided and metabolites with FDR<0.1 were considered to be significant.

Supplementary Table ST10: Raw MRM lipidomics data of Aβ- vs. vehicle-treated primary microglial cell conditioned media at 1 and 24 hours. The table lists the MRM transitions screened for TAGs and the respective ion intensity values at two different time points, organized by MRM transition.

Supplementary Table ST11: Pathway analysis for cell metabolites at 1, 12, and 24 hours of Aβ- vs. vehicle-treated primary microglia cultures. List of all pathways matched to the differentially-expressed metabolites (FDR<0.1) are highlighted in the tables. The pathways with P<0.05 were considered to be significant and are highlighted in the scatter plots in the supplementary figures.

Supplementary Table ST12: Pathway analysis for media metabolites at 1, 12, and 24 hours of Aβ- vs. vehicle-treated primary microglia cultures. List of all pathways matched to the differentially-expressed metabolites (FDR<0.1) are highlighted in the tables. The pathways with P<0.05 were considered to be significant and are highlighted in the scatter plots in the supplementary figures.

SUPPLEMENTARY MOVIE LEGEND

Supplementary Movie 1: 3D rendered plaque-proximal microglia show increased LDs in human AD patients. Representative confocal z-stack for which 3D "Surfaces" were made in Imaris for IBA1, PLIN2 and AmyloGlo channels. Only LDs in microglia (red) are shown. Plaque-proximal microglia (yellow) defined by a 0-10μm distance from the closest plaque (purple) contain increased LDs (red) compared to plaque-distant (>10μm from closest plaque) LD+ microglia (green). Plaque-proximal LD- microglia are also shown in orange.

STAR Methods

Animals
C57BL/6J and 5xFAD mice were obtained from the Jackson Laboratory and were maintained in a pathogen free facility. All experiments involving mice were performed in accordance with the Purdue University's Institutional Animal Care and Use Committee (IACUC) guidelines.

Primary mouse microglia isolation and culture from adult mouse brains
Primary microglia from adult mouse brains were isolated and cultured per a previously-described protocol[43]. Briefly, CD11b+ primary microglia were isolated from adult mice (both male and female) and cultured as described previously[43]. Mice were euthanized with CO_2 according to IACUC guidelines, and perfused brains were removed and cut into small pieces before

27

984 homogenization in 1x Dulbecco's phosphate-buffered saline with Calcium and Magnesium
985 (DPBS^{++}) with 0.4% DNase-I on the tissue dissociator at 37 ^{o}C. After filtering the cells through a
986 70-µm filter, myelin was first removed using Percoll PLUS reagent (GE Healthcare #45001754),
987 then again by using myelin removal beads. After myelin removal, CD11b$^+$ cells were selected from
988 the single-cell suspension using the CD11b beads (Miltenyi) as per the manufacturer's instructions.
989 The CD11b$^+$ cells were finally resuspended in microglia growth media[68], further diluted in TIC
990 (TGF-β, IL-34, and cholesterol containing) media with 2% FBS (Atlanta Biologics #S11150, Lot
991 #H17115) before seeding 1x10^5 cells per 500 µL in a well of a 24-well plate (Falcon). The cells
992 were maintained in TIC media at 37°C and 10% CO$_2$, with media being changed every other day
993 until the day of Aβ treatment (around 12-14 days *in vitro* (d.i.v.)).

994

995 **Aβ preparation**
996 The solid human Aβ1-42 peptide (Anaspec #20276) was prepared per our previously-described
997 protocol[69]. Briefly, the peptide was dissolved in 20 mM NaOH, pH=10.5 to make ~100 µM stock
998 solution. Peptide aggregation was initiated by incubating the solution at 37°C for 24 hours. The
999 peptide was then either stored at -80°C or used directly on the cells after being diluted in culture
1000 medium and filtered through a 0.22 µm syringe filter.

1001

1002 **Treatment of Aβ**
1003 Primary microglia were treated with 500 µL/well of 500 nM Aβ1-42 or vehicle for 1, 12, or 24
1004 hours. After the respective time points, the conditioned media (CM) from each well was collected
1005 and stored at -80°C. The cells were then detached from wells with 0.25% trypsin and collected in
1006 1x phosphate-buffered saline (PBS) before pelleting at 500 x*g* for 6 mins at 4°C. The supernatant
1007 was aspirated, and pellets were also stored at -80°C along with the CM for direct injection-MS/MS
1008 and MRM-profiling.

1009

1010 **Lipid extraction by the Bligh & Dyer method**
1011 Lipid and metabolite extracts were prepared using a slightly modified Bligh & Dyer extraction
1012 procedure[70]. The frozen cell pellets from primary microglia were thawed at room temperature, and
1013 ultrapure water, methanol, and HPLC-grade chloroform were added to the pellets. The samples
1014 were vortexed, resulting in a one-phase solution that was then incubated at 4°C for 15 mins. Next,
1015 ultrapure water and chloroform were added, resulting in a biphasic solution. The samples were
1016 centrifuged at 16,000 x*g* for 10 mins, resulting in 3 phases in each tube. The bottom organic phase
1017 containing the lipids were transferred to new tubes, while the middle phase consisting of proteins
1018 and the upper polar phase were discarded. The solvents from the organic phase were evaporated
1019 in a speed-vac. The dried lipid extracts were dissolved in acetonitrile/methanol/300 mM
1020 ammonium acetate (3:6.65:0.35 v/v/v). The lipid extract solutions were diluted further 50 times
1021 before running them on a mass spectrometer.

1022

1023 **Unbiased lipidomic and TAG-species profiling using MRM-profiling**
1024 To determine if there were differences in lipid profiles that occur with Aβ activation over 24 hours,
1025 lipids extracted from cell lysates as well as conditioned medium were processed for Multiple
1026 Reaction Monitoring (MRM)-profiling[71,72]. Instruments used in these experiments are listed in the
1027 supplemental material. The detailed methodology of MRM-profiling for targeted lipid profiling
1028 has been described previously[73]. This method enabled the interrogation of the relative amounts of
1029 numerous lipid species within ten major classes of lipids based upon the LipidMaps database[74].

1030 The lipid classes, along with the total number of MRM transitions screened, are presented in **Fig.**
1031 **S1b**. Due to the large number of triacylglycerol (TAG) lipid species interrogated in this study,
1032 TAGs were run in two separate methods (TAG 1 and TAG 2), each measuring relative ion
1033 transitions for different TAG species. The TAG species measured in each method were arbitrarily
1034 divided. For sample preparation, dried lipid extracts were diluted in methanol:chloroform (3:1 v/v)
1035 and injection solvent to obtain a stock solution. Then, the diluted lipid extract was delivered to the
1036 ESI source of an Agilent 6410 triple quadrupole mass spectrometer to acquire the mass
1037 spectrometry data by flow injection (no chromatographic separation). The raw MS data obtained
1038 were processed using an in-house script, and the lists containing MRM transitions along with the
1039 respective ion intensity values were exported to Microsoft Excel for statistical analyses to identify
1040 the significant lipids and metabolites in Aβ-treated versus vehicle-treated microglia. Individual
1041 TAG species were also profiled in primary cultured microglial cells treated with Aβ and vehicle
1042 controls, as well as 5xFAD and WT acutely-isolated microglia using MRM-profiling methodology
1043 as described above. Briefly, diluted lipid extracts were directly infused into the Agilent Jet Stream
1044 ion source of an Agilent 6495C triple quadrupole mass spectrometer. TAG molecular species were
1045 identified based upon previously-established MRMs.

Statistical analyses for lipidomics and metabolomics

1048 Statistical analyses were performed according to our recently-published study[75]. The edgeR
1049 package[76] was used for Aβ- versus vehicle-treated microglia comparisons, as well as comparisons
1050 of 5xFAD vs. WT microglia. Abbreviation "s" was used to denote sample, which represent
1051 different replicates of an analyte class and "b" was used to indicate a biomarker such as a single
1052 lipid or metabolite. Ion counts of a biomarker were denoted using these two subscripts. The
1053 experimental blank that was done with the injection media was modeled as an 'intercept' sample
1054 in the analysis to make certain that comparisons were significant with respect to the blank. A
1055 generalized linear model was fitted using the edgeR package[76] for the mean variance as follows:

$$\log \mu_{bs} = X_s^T \beta_b + \log N_s$$

1059 Here, N_s represents the sum of all ion intensities for the sample s. The coefficient of variance (CV)
1060 for a biomarker ion counts in a sample (y_{bs}) can be calculated using the following equation:

$$CV^2(y_{bs}) = 1/\mu_{bs} + \Phi_b$$

1064 Dispersion of the biomarker was denoted as Φ_b and it was estimated using the common dispersion
1065 method[77]. The associated log-fold change was calculated between the Aβ-treated and vehicle-
1066 treated microglia and p-values were obtained using the likelihood ratio test. The BH method was
1067 used to calculate p-values to acquire false discovery rates (FDRs)[78] and a lipid or a metabolite was
1068 considered to be significant if fold change > 0.5 and FDR < 0.1.

Lipid droplet staining of acutely-isolated microglia in suspension

1071 CD11b⁺ cells were isolated from male and female mice (3-4 or 5-7 months old; 5xFAD or WT)
1072 and resuspended in 1x PBS, counted using a hemocytometer (1:10 ratio of trypan blue to cell
1073 suspension) and stained with 2 μM BODIPY in 1x PBS for 1 hour at 37°C. The cells were then
1074 washed once, resuspended in 1x PBS and taken for analysis on an Attune NxT flow cytometer
1075 (Invitrogen) after staining of dead cells with DAPI.

29

1076
Perfusion and tissue processing
Mice were euthanized with CO_2 and transcardially perfused with PBS and 4% paraformaldehyde (PFA). Brains were extracted and coronally sectioned (50 µm) using a vibratome and stored in antigel solution (30% glycerol, 30% ethylene glycol, in PBS) at -20°C until use for IHC staining.

Immunohistochemistry and staining
Free-floating sections were washed five times in PBS, followed by incubation with Methoxy X04 (10µM, Tocris Bioscience,) solution in PBS for 15 minutes. Sections were then stained with HCS LipidTox Green Neutral Lipid Stain (1:1000, ThermoFisher) in PBS for 15 min, followed by incubation with antigen retrieval buffer (10mM sodium citrate, 0.05% Tween20, pH=6.0) at 70°C for 40 min. The sections were allowed to cool, washed, and treated with 0.1% NaBH4 for 30 min. Following antigen retrieval, sections were blocked with blocking buffer (5% NGS, 0.01% Triton X-100, in PBS) for 1 hr at room temperature. The sections were then incubated overnight with the following primary antibodies: anti-IBA1 (1:150, Millipore Sigma) anti-DGAT2 (1:150, ThermoFisher) in blocking buffer at 4°C. Post-incubation, sections were washed thoroughly with PBS + 0.01% Triton X-100 and incubated with secondary antibodies: Goat anti-Mouse Alexa Fluor 594), Goat anti-Mouse Alexa Fluor 647 and Goat anti-Rabbit Alexa Fluor 594 (all from Invitrogen and diluted at 1:500) for 1.5 h at room temperature. Following washes with PBS + 0.01% Triton X-100, sections were mounted on slides, allowed to dry, and coverslipped using Fluoromount-G anti-fade mounting medium (Southern Biotech).

***Ex-vivo* Lipid droplet staining and Aβ phagocytosis assay of acutely-seeded microglia**
Following the protocol described above for cell isolation, 100K CD11b$^+$ cells from 5-7-month-old female C57BL/6J mice were seeded in TIC media for 1 hour, followed by 500 nM Aβ^{pH} (in TIC media) / vehicle treatment for 30 minutes. Post-treatment, the cells were stained with LipidTox (1:200) in 1xPBS for 30 minutes at 37°C. After staining, the cells were washed with 1x PBS, detached, and collected in ice-cold 1x PBS. Three minutes before analysis of each sample, DAPI was used to stain dead cells. Single positive controls, gating strategies and analyses were done as described above, but for this experiment live LipidTox$^+$ or LipidTox$^-$ cells were identified on the Alexa-Fluor 647 channel, while Aβ^{pH+} and Aβ^{pH-} cells were identified on the FITC channel on an Attune NxT flow cytometer (Invitrogen).

Treatment of DGAT2 inhibitor (D2i) and *ex-vivo* lipid droplet staining and Aβ phagocytosis assay of acutely-seeded microglia
The above protocol was followed with slight modifications for D2i (PZ0233, Sigma) treatment. Briefly, CD11b$^+$ cells were seeded TIC media containing 15 µM D2i / vehicle for 1 hour, followed by 500 nM Aβ^{pH} (in TIC media) / vehicle containing 15 µM D2i / vehicle treatment for 30 minutes. Post-treatment, the cells were washed with 1xPBS and stained with LipidTox (1:200) containing 15 µM D2i / vehicle in 1xPBS for 30 minutes at 37°C. After staining, the cells were washed with 1x PBS, detached, and collected in ice-cold 1x PBS containing 15 µM D2i / vehicle and analyzed on the flow cytometer.

Sample	Aβ^{pH}	LipidTox	D2i
LipidTox only	-	+	-
Aβ^{pH} only	+	-	-

Aβ^{pH} + LipidTox	+	+	-
LipidTox+ D2i	-	+	+
Aβ^{pH} + LipidTox+ D2i	+	+	+

Dgat2 **mRNA expression by PCR**

CD11b$^+$ cells isolated from 5-7-month-old female mice (5xFAD and WT) were resuspended in 1x PBS, counted using a hemocytometer (1:10 ratio of trypan blue to cell suspension) and stored at -80 °C until next step. Total RNA was isolated and purified by using Quick-RNA Miniprep Kit (Zymo Research) following the manufacturer's protocol. RNA quantification and purity were assessed using Varioskan LUX imaging multi-mode reader (Thermo Scientific). Real-time PCR was conducted using TaqMan probes (Applied Biosystems, Foster City, CA) for Dgat2 (Mm00499536_m1) and the mouse housekeeping gene β-actin (Mm00607939_s1) as an endogenous control. For PCR amplification, an initial denaturation at 95°C for 15 min was followed by 40 cycles of denaturation at 95°C for 10 s and annealing at 60°C for 1 min. Reactions were run in duplicate. Open qPCR software version 1.0.2 (Chai Biotechnologies Inc.) was used for post-amplification analysis. Cq and Tm values were calculated directly by the instrument software and used for finding fold change for *Dgat2* gene expression in 5xFAD relative to WT by the comparative $2^{-\Delta\Delta CT}$ method.

Stimulated Raman Scattering (SRS) microscopy for label-free lipid droplet imaging

A dual-output 80-MHz femtosecond pulsed laser source (InSight X3+, Spectra-Physics) was used for the excitation of SRS. The wavelength-tunable output (680-1300 nm) was used as the pump beam and the 1045 nm fixed-wavelength output was used as the Stokes beam. The pump beam was tuned to 800 nm to image CH vibrations in brain samples. Both beams had a pulse duration of ~120 fs. The Stokes beam was directed into an acousto-optic modulator (ISOMET, M1205-P80L-0.5), which was controlled by a radio frequency driver (ISOMET, 522B-L) and modulated by a function generator (DG1022Z, Rigol). A square wave of 2.5 MHz and 50% duty cycle was used for laser intensity modulation. The 0th order laser beam from the AOM was used for excitation. The beams were combined spatially by a dichroic beam splitter and were chirped using glass rods (SF57, Lattice Electro-Optics). One 150 mm rod was placed only in the probe beam pathway, while two 150 mm rods were used after combining the two beams. We bent the optical beam path to double-pass the two chirping rods to increase the chirping. This gives a 1+4 (Stokes + combined) chirping configuration, which chirps the pump beam to 3.4 ps and the Stokes beam to 1.8 ps. The laser power used on the sample was ~ 15 mW for the pump and ~30 mW for the Stokes beam. A motorized linear translational stage (X-LSM050A, Zaber Technology) was used to scan the optical delay between pump and Stokes beams, which were converted to Raman shifts by spectral focusing. The optical delay scanning steps were 10 µm per step. The combined beams were scanned by a 2D galvo scanner set (GVS002, Thorlabs) installed to an upright microscope for imaging. A 60x/1.2 NA water immersion objective lens (UPLSAPO 60X, Olympus) was used to focus the beams onto the sample. The SRS signal was collected by a 1.4 NA oil-immersion condenser. The pump beam was detected with a photodiode detector (S3994, Hamamatsu) with a short-pass filter (980 SP, Chroma technology) to reject the Stokes beam. The alternate voltage signal was amplified using a lab-built tuned amplifier centered at 2.5 MHz. The SRS signal was extracted using a lock-in amplifier (HF2LI, Zurich Instruments). A 2D translation stage (H101, ProScan III, Prior Technology) was used to control sample positions and to perform automated large-area image acquisition and stitching. Data acquisition was enabled using a high-speed data

31

1162 acquisition card (PCIe 6363, National Instruments). The laser scanning and image acquisition was
1163 performed by custom-written software based on LabVIEW.
1164

Analysis of SRS microscopy data
1166 For analysis, the images were saved in .txt files and processed using ImageJ. Pseudocolors were
1167 used to display different chemical compositions. Hyperspectral images were used to obtain spectra
1168 of lipid droplets and other chemical compositions of the tissue. The spectral profiles were
1169 normalized by using a laser intensity profile obtained from cross-phase modulation. For
1170 quantitative image analysis a Gaussian blur filter (r=3) was used to process the original image.
1171 Then, the processed image was subtracted from the original image to highlight the lipid droplets.
1172 Intensity thresholding and particle analysis were then performed using ImageJ built-in functions
1173 for quantitative lipid droplet analysis. For quantitative analysis results, areas from the WT and
1174 5xFAD sections were selected and the lipid droplets were analyzed within each area. Merging of
1175 different image channels was performed using ImageJ. The percentage was calculated by dividing
1176 the number of pixels corresponding to LD signal by the total number of pixels of the entire image.
1177

Saturated fatty acid structure elucidation using gas-phase ion/ion chemistry
1179 Utilizing gas-phase ion/ion chemistries, the detailed structural elucidation of complex lipids in
1180 biological mixtures has been demonstrated previously[79,80]. Here, a charge inversion ion/ion
1181 reaction strategy was employed to examine the structure of saturated fatty acids. All experiments
1182 were conducted on a Sciex QTRAP 4000 triple quadrupole/linear ion trap mass spectrometer
1183 (SCIEX, Concord, ON, Canada) that has been modified to perform ion/ion reactions[81]. To facilitate
1184 the mutual storage of oppositely-charged ions, the key instrumental modifications involve the
1185 ability to apply AC voltages to the end plates of the q2 reaction cell. Alternately, pulsed
1186 nanoelectrospray ionization (nESI) emitters permit the sequential injection of tris-phenanthroline
1187 magnesium reagent dications and fatty acid analyte anions[82]. Singly-deprotonated fatty acid
1188 anions, denoted $[FA - H]^-$ anions, generated via direct negative nESI of the lipid extract or
1189 authentic reference standard were mass-selected with unit resolution during transient through Q1
1190 and subsequently transferred to the high-pressure collision cell, q2, for storage. Next, positive nESI
1191 produced tris-phenanthroline magnesium dications, denoted $[MgPhen_3]^{2+}$, which were isolated in
1192 Q1 prior to accumulation in the reaction cell q2. The $[FA - H]^-$ anions and $[MgPhen3]2+$ reagent
1193 dications were then mutually stored in q2, yielding the $[FA - H + MgPhen_2]^+$ complex cation.
1194 Energetic transfer from the reaction cell q2 to the linear ion trap (LIT), Q3, resulted in the neutral
1195 loss of a single phenanthroline ligand and the generation of the charge-inverted complex cation
1196 referred to as $[FA - H + MgPhen]^+$. Following mass-selection in Q3, the analysis of charge inverted
1197 product ions was performed using single-frequency resonance excitation, commonly referred to as
1198 ion-trap collision-induced dissociation (CID) (q = 0.383). In summary, reproducible spectral
1199 patterns facilitate fatty acid identification[79]. In all cases, mass analysis was performed using mass-
1200 selective axial ejection (MSAE)[83].
1201

Pathway analysis for metabolomics data
1203 Metabolomic pathway analysis was performed using the MetPA[84] (metabolomics pathway
1204 analysis) tool on MetaboAnalyst 5.0: a free, web-based tool for metabolomics data analysis that
1205 uses the KEGG metabolic pathways as the backend knowledge-base. The differentially-regulated
1206 metabolites (FDR<0.1) were uploaded into the compound list with hypergeometric test as the
1207 enrichment method and relative-betweenness centrality for topology analysis. The KEGG pathway

1208 library for *Mus musculus* was chosen as the reference database. All of the matched pathways
1209 according to the p values from the pathway enrichment analysis and pathway impact values from
1210 the pathway topology analysis were visualized using the "metabolome view" scatter plot.
1211

Human brain tissue staining

1213 Human hippocampal formalin-fixed paraffin-embedded (FFPE) tissue sections from autopsy
1214 samples of both male and female Alzheimer's disease (AD) patients (>74 years, n=3 per sex) and
1215 non-symptomatic (NS) cases (>62 years, n=3 per sex) were used. NS cases were obtained from
1216 individuals without any neurological or psychiatric diagnosis, and no chronic systemic
1217 inflammatory or infectious condition. All human post-mortem tissue was obtained from the
1218 Pathology Research Core in the Robert J. Tomsich Pathology and Laboratory Medicine Institute
1219 of the Cleveland Clinic. Institutional ethical guidelines were followed for the appropriate use of
1220 these fully de-identified samples for research purposes, after IRB approval. All tissue samples
1221 were cut at 15 μm and standard de-paraffinization procedures in xylene and decreasing
1222 concentration ethanol solutions were utilized. Sections were stained for amyloid plaques using
1223 Amylo-Glo RTD Amyloid Plaque Stain Reagent (Biosensis) according to the manufacturer's
1224 instructions. Then antigen retrieval was performed in 10mM Tris / 1mM EDTA buffer (pH=8.0)
1225 for 20 min at 97°C. After cooling down to room temperature, sections were rinsed with distilled
1226 water and blocked in 10% normal donkey serum in PBS-Tween-20 0.05% (v/v) for 1 hour. Primary
1227 antibodies were added in blocking buffer and sections were incubated for 72hr at 4°C (anti-
1228 Adipophilin (PLIN2 Fitzgerald Industries International, 1:200); rabbit anti-DGAT2,
1229 (ThermoFisher, 1:200); anti-IBA1, (Millipore, 1:200). Sections were washed with PBS-T 0.05%
1230 (v/v) and incubated with secondary antibodies in blocking buffer for 2h at room temperature
1231 (Jackson Immunoresearch: donkey anti-guinea pig AF594, 1:500; donkey anti-rabbit FITC,
1232 1:1000; alpaca anti-mouse Cy5, 1:100). Autofluorescence was quenched with TrueBlack-
1233 Lipofuscin autofluorescence quencher (Biotium) according to the manufacturer's instructions and
1234 sections were coverslipped with anti-fade fluorescence mounting medium (Abcam). Imaging was
1235 performed using a Zeiss LSM 800 confocal microscope using a 40x 1.3NA oil immersion lens and
1236 quantification of lipid droplets in relation to microglia and amyloid plaques was performed using
1237 the surfaces module in Imaris 9.8.2 (Bitplane).
1238

Image processing

1240 Confocal microscopy images in Figures **1i**, **2c** and **4b** were processed using Imaris 9.8.2 (Bitplane)
1241 to reduce noise by applying the Gaussian or Median filters. For **1i** and **2c**, remaining non-specific
1242 speckles in the IBA1 channel (likely produced during the antigen retrieval and
1243 immunofluorescence protocol) were removed by size exclusion of 3D objects smaller than 1 or 2
1244 μm^3 using the Imaris tool "surfaces". A similar approach was also used for confocal microscopy
1245 images acquired from human post-mortem FFPE tissue sections that often show artefacts from the
1246 deparaffinization and antigen retrieval protocols. 3D objects smaller than 2 or 3 μm^3 (for IBA1)
1247 and 1 μm^3 (for PLIN2) were removed using Imaris. This size exclusion of speckles and artifacts
1248 also ensured that only true LD particles were selected for visualization and quantification in the
1249 PLIN2 channel. For the DGAT2 channel, only the Gaussian filter was applied to reduce noise. The
1250 mouse brain confocal microscopy images were processed using ImageJ and the despeckle tool was
1251 used to remove the fine noise / grainy speckles from the images prior to being used for LD
1252 quantification using the 'Analyze particles' function coupled with the ROI manager tool.
1253

1254 **Statistical analyses**

1255 Data collection was randomized for all experiments and experimenters were blinded for imaging
1256 and data analyses. All statistical analyses were performed using GraphPad Prism version 8.2.1 or
1257 on R version 4.1.2. Mean between two groups were compared using two-tailed unpaired Student's
1258 t-test. Data from multiple groups were analyzed by one-way analysis of variance (ANOVA) with
1259 Tukey's multiple comparison tests. Information on the sample size, numbers of replicates and
1260 statistical test used for each experiment is included in the figure legends.
1261
1262
1263